

ALBERT-LUDWIGS-UNIVERSITÄT FREIBURG

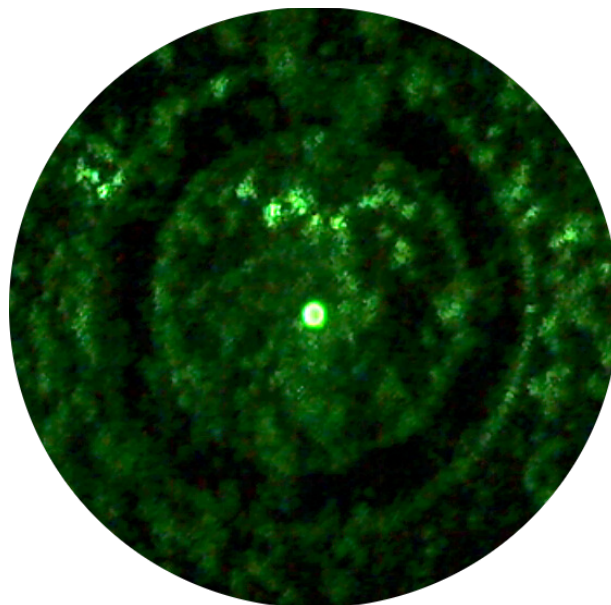
PHYSIKALISCHES INSTITUT

MASTER THESIS

Benchmarking Micro-Diamonds for Sensing Applications

Author:
Deviprasath PALANI

Supervisor:
Prof. Dr. Tobias SCHAETZ



January 10, 2019

UNI
FREIBURG



Erklärung

Ich versichere hiermit, dass die vorliegende Masterarbeit selbstständig verfasst und keine weiteren als die angegebenen Hilfsmittel benutzt sowie die Stellen der Arbeit, die in anderen Werken dem Wortlaut oder dem Sinn nach entnommen sind, durch Angaben der Quellen sichtbar gemacht wurden. Außerdem versichere ich, dass die vorgelegte Masterarbeit nicht Bestandteil eines anderen Prüfungsverfahrens ist und war.

(Ort, Datum)

(Unterschrift)

Abstract

Local probing in the order of sub-micro/nano-meter proximity, has a wide range of applications in biology, nanotechnology, etc. we assemble a benchmark setup consisting of a confocal microscope and a data acquisition system, capable of accessing an ensemble of NV^- centers within micro-sized diamonds placed on the coplanar waveguide under ambient conditions. We characterize our experimental setup and demonstrate control over the electronic degrees of freedom of the NV^- with a spatial and temporal resolution of $\sim 0.3 \mu\text{m}$ and $\sim 1 \text{ ns}$ respectively. The orientation of the diamond crystal's [111] plane is deduced within $\sim 10 \%$ uncertainty with respect to the lab frame of reference. The influence of stray and control fields on the NV^- centers are studied, to characterize the systematics of the apparatus. By optimizing the control fields, time-critical quantum control sequences are performed and the coherence times of the addressed electronic states are measured to be about $\sim 0.30 \mu\text{s}$. Henceforth, our setup can be used to benchmark alternate levitation methods to harness the full potential of the spatially controlled quantum sensor.

Contents

1	Introduction	9
2	Methods	11
2.1	Properties of Nitrogen Vacancy defects in diamonds	11
2.2	Experimental Set-up	15
2.2.1	Data acquisition system(ARTIQ) and Microwave transmission	15
2.2.2	Confocal Imaging	18
2.3	Calibration	20
2.3.1	Frequency Quadrupling Circuit	20
2.3.2	Diode Laser and Digital Modulation	22
2.3.3	Imaging optics	24
2.3.4	Spectrometer	26
2.3.5	Magnetic Field	28
3	Results	31
3.1	NV ⁻ Identification	31
3.2	Influence of Laser power on Ground State Spin Dynamics	35
3.3	Magnetic field sensing and Orientation of NV centers	38
3.4	Rabi Oscillations	42
4	Discussion and Outlook	45
	Appendix	45
A	Spin-strain interactions	46
B	Estimation of NV orientations with the help of Zeeman effect	47
C	Python codes [Kernel and Host code]	48
D	Power-Current calibration curve	51
	Bibliography	55
	Acknowledgements	56

Chapter 1

Introduction

Diamonds are popular as a gemstone and best known for their high mechanical hardness, chemical inertness and heat conductivity, leading to many industrial applications. Though the diamonds are optically transparent, they do occur in different colours due to the presence of fluorescent lattice substitutional defects[1–3]. These fluorescent diamonds with the non-cytotoxicity property, due to their chemical inertness are preferred as fluorescent markers in many biological applications. A particular defect with nitrogen atoms, known as Nitrogen-Vacancy centre (NV^- centre) is used as a bio-marker; as well as a sensor due to its quantum mechanical properties[4, 5]. These NV^- centres have been demonstrated to be sensitive to external disturbances such as electric, magnetic, temperature and pressure[6–15]. The quantum methodologies[16–18] developed in the last century, enables high-precision measurements and quantum information processing using such a quantum mechanical system. Realization of such a system for metrology using ions or atoms, require high isolation from environmental disturbances. The quantum nature of the NV centers is well protected by the diamond lattice structure. The packaging naturally isolates the system sufficiently from disturbances and ensures access to its quantum nature. Thereby, making the metrological properties of the NV^- centers to be available even under ambient conditions. Micro- or nano-sized diamonds with NV^- defects are suitable sensor packages for sensing in sub-nanometer proximity.

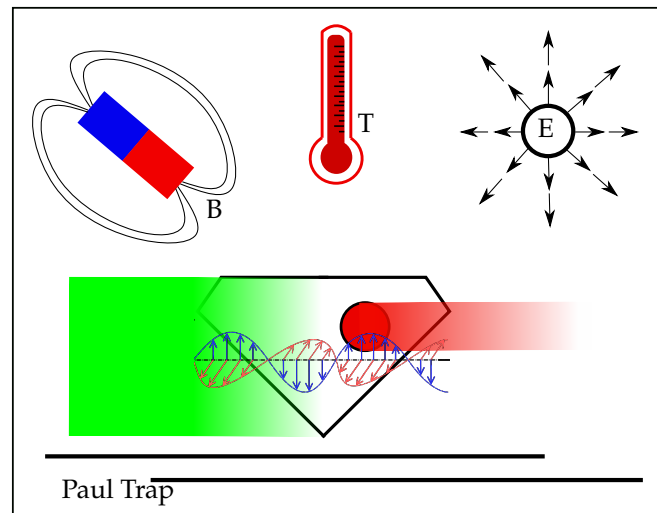


Figure 1.1: **Artistic representation of Diamonds with NV centers and its interactions.** A diamond with a NV defect is trapped with a Paul trap, where the quantum states are addressed using control fields such as optical(Green - Excitation, Red - Fluorescence) and Microwave fields. The identified quantum states are perturbed due to external disturbances such as Magnetic, temperature and electric fields. Such influences are quantified using various quantum techniques.

The quantum states of the NV^- centre need to be addressed or manipulated to harness the sensing properties. This is ensured through the optical and microwave fields as shown in Fig. 1.1. Using time-critical experimental methodologies, the preferred electronic states (spin manifolds) are chosen for sensing applications. The magnetic field sensing is demonstrated

with a sensitivity of few $\text{fT}/\sqrt{\text{Hz}}$ for static magnetic field case[7]. Similarly, the static electric field is measured with sensitivity of $5.8 \text{ kV cm}^{-1}/\sqrt{\text{Hz}}$ [8], temperature with $0.13 \text{ K}/\sqrt{\text{Hz}}$ [19], and pressure with $0.6 \text{ MPa}/\sqrt{\text{Hz}}$ [20] under ambient conditions.

Using these micro-, nano-diamonds as a scanning tip in an atomic force microscopy enables high-precision field sensing in close proximity. In biological conditions, such as intra-cellular or micro-fluidic channel environments[21], a mechanically fixed sensor is of less use. Sensing and spatial control over the micro-diamonds in such conditions, are demonstrated using optical tweezers[22–28], where the orientation control is enabled using radiation pressure of the laser beam. Various Paul trap designs are demonstrated to levitate diamonds[29–31] with the help of surface charges using an oscillating electric potential[32]. Using paul trap, the spatial stability and access to the internal degrees of freedom of the NV^- centers within levitated diamonds are demonstrated[30, 33]. As shown in Fig.1.1, we envision a compact device with electromagnetic trap that can control the external degrees of freedom of a trapped diamond via configurable control potentials[34–36] along with ability to control the fields to address the internal degrees of freedom. Thereby, the spatial control along with ability to address the internal degrees via quantum methodologies used in field of atomic physics, can enable us to use micro/nano-diamonds as a robust spatially controlled quantum sensor.

In this report, foremost, we establish a benchmark set-up as mentioned in Sec. 2.2, to address quantum states of the NV^- centres and can also be integrated to perform levitation techniques. The experimental set-up comprises of a data acquisition system (DAQ) as shown in Sec. 2.2.1, is controlled via FPGA[37] along with a confocal imaging optics[38] as shown in Sec. 2.2.2, to execute quantum methodologies for sensing applications and information processing[39]. Secondly, the chosen micro-diamonds are used to characterize the intrinsic quantum properties of the NV^- centers and in optimizing the experimental setup to perform time-critical quantum control sequences as shown in Sec. 3.4.

Chapter 2

Methods

In this chapter, we discuss the properties of the NV⁻ centers in the micro-diamonds. Followed by, description of the experimental set-up and characterization of various components in it.

2.1 Properties of Nitrogen Vacancy defects in diamonds

Diamonds are known for their hardness, due to the covalent bonds formed between the carbon atoms. They are classified in Fd3m space group and grouped under face-centered cubic bravias lattice. In spite of its transparency in the visible region of the electromagnetic spectrum, they occur in different colors due to the presence of impurities in their crystal structure. Occurrence of impurities like germanium, silicon, nitrogen, etc. are called color defects or point defects[40]. A Nitrogen-vacancy site is a combination of substitutional and vacancy defect, where a carbon atom is replaced by a nitrogen atom along with an absence of carbon atom in the adjacent site. The axis connecting the substitution nitrogen impurity with an adjacent vacancy site in the diamond lattice occurs in eight different orientations. Using space group properties, these orientations are represented using four different Miller indices as shown in Fig 2.1. The nitrogen vacancy center occurs as positive, negative and neutrally charged variants. In the case of negatively charged NV, the molecular orbital formation with the sp³ dangling bonds from three adjacent carbon atoms and the nitrogen atom captures an electron in the system. Along with three carbon atoms near the vacancy, the overall system with NV⁻ can be formulated in terms of six electron model[41] and represented as C_{3v} symmetry as shown in Fig 2.3a. The presence of an extra electron in the system makes it negatively charged and also para-magnetic with an integral spin of one.

Figure 2.2 shows the electronic structure of the NV⁻[42] consists of two triplet states, ³A₂ ground state and ³E excited state[43] separated by 1.945 eV, along with two other singlet states E₁ and A₁ with energy levels between the two distinguished triplet states. According to the Frank-Condon principle, the presence of lattice vibrations contribute phonon energy levels to the existing distinguished triplet states. The allowed transition from the excited triplet state to the ground state emits visible spectra that spans from ~550 - 800 nm. The transition between the vibronic ground states to the triplet electronic states (³E and ³A₂) corresponds to the Zero-Phonon Line (ZPL). The ZPL in the case of NV⁻ occurs at ~637 nm. In addition, the broad spectra contains vibronic energy transitions.

The localized electronic states to the NV⁻ center and the C_{3v} symmetry of the point defect helps in constructing the molecular orbital theory with Linear Combination of Atomic Orbital (LCAO). This LCAO method is an approximation to understand the energy ordering of the molecular orbitals (MO's)[42]. This method doesn't discuss the influence of external fields on the fine structure of the defect. Therefore, the interactions on the ground state of the defect due to external perturbations are approximately decoupled with the help of canonical spin-Hamiltonian formalism and the far-off resonance mechanism is chosen to excite the NV⁻ centers.

$$H_{gs} = \frac{1}{\hbar^2}(D_{gs} + d_{||}E_z)S_z^2 + \frac{\mu_b}{\hbar}g\bar{S}\cdot\bar{B} - \frac{1}{\hbar^2}d_{\perp}E_x(S_x^2 + S_y^2) + \frac{1}{\hbar^2}d_{\perp}E_y(S_xS_y + S_yS_x) \quad (1)$$

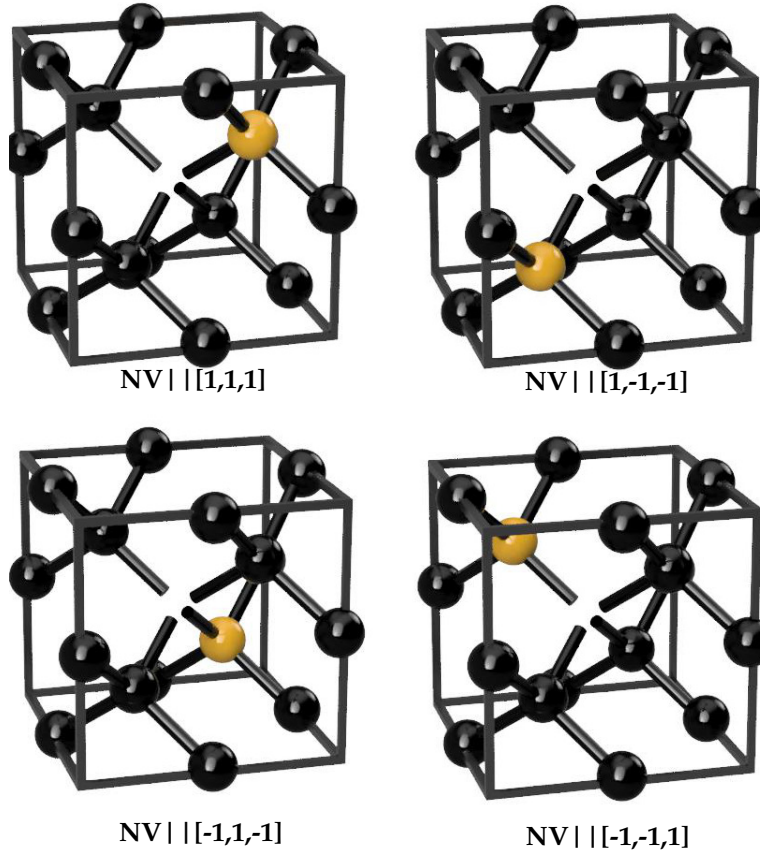


Figure 2.1: **Schematic of the Diamond cubic lattice structure with NV center.** Carbon atoms (Black) form covalent bonds with other carbon atoms, resulting in a face centered bravias lattice structure. The presence of nitrogen atom (Yellow) in the place of carbon atom along with an adjacent vacancy site; this combination of substitutional and vacancy defect makes NV center. The sp^3 dangling bonds from neighboring carbon atoms, gives C_{3v} symmetry to the point defect. Four different schematics show the Miller indices representation of probable orientations of the NV centers in the crystal structure.

The interaction part of the overall Hamiltonian that represents the ground state of the NV⁻ center, has contributions from the magnetic, electric, strain fields and hyperfine splitting[44] due to the presence of isotopes with non-integral nuclear spins like C^{13} and N^{15} near the vacancy. The Born-Oppenheimer approximation is used to decouple the interaction terms as shown in Eqn. 1. From the Equation 1, the Z-components represent the interactions corresponding to axial direction¹ and the X, Y corresponds to non-axial interactions. The spin components are represented with S_x , S_y , S_z . The electric field interactions along with strain interactions are accounted by E. The $d_{||}^2$ and d_{\perp}^3 [8] represents the piezoelectric coupling constant in axial and non-axial directions. D_{gs} represents the zero-field splitting in the ground state spin. The first term represents the zero-field splitting D_{gs} along with a contribution of electric and strain field interactions in the axial direction Z. The second term deals with the Zeeman splitting due to the interaction of magnetic field perturbation. This Zeeman formulation is valid until 0.1 Tesla due to the occurrence of non-homogenous splitting followed by an anti-crossing of energy level at magnetic field of ~ 1024 G in axial direction[45]. The third and fourth terms represent the interaction of electric and strain fields in non-axial directions with respect to C_{3v} symmetry.

¹Parallel to NV⁻ axis

² $d_{gs}^{\parallel}/h = 0.35 \pm 0.02 \text{ Hz cm V}^{-1}$

³ $d_{gs}^{\perp}/h = 17 \pm 3 \text{ Hz cm V}^{-1}$

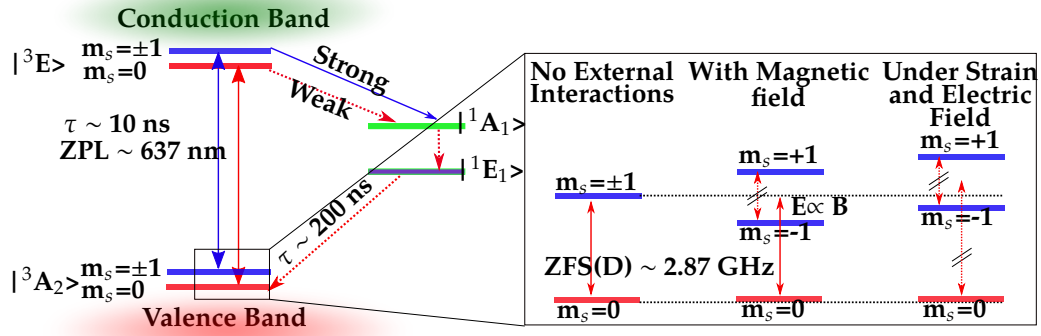


Figure 2.2: **Schematic of electronic structure of NV^- center.** The $|^3\text{A}_2\rangle$ and $|^3\text{E}_3\rangle$ are the triplet ground and excited state respectively. Solid lines with arrows represent strong transitions, dashed lines represent weak and non-radiative transitions. The excited state has a lifetime of ~ 10 ns, the radiative transition results in a broad optical spectra that spans 550 nm - 800 nm. The radiative transition without phonon contribution occurs at ~ 637 nm, called as zero-phonon line, ensures the presence of NV^- . The radiative and inter-system crossing non-radiative decay mechanisms populates $m=0$ manifold of the ground state spin. The lift in degeneracy in case of both ground and excited triplet state corresponds to the zero-field splitting. In the ground state spin, ZFS or D_{gs} occurs at ~ 2.87 GHz at ideal case with no external perturbations. While interaction with static magnetic field, the degeneracy in $m=\pm 1$ states are lifted and proportional to the applied field strength. As a consequence, E-Parameter varies symmetrically across the ZFS frequency. In case of external strain and electric field, the consequences occurs in form of shift in D- and E-parameters. The shifts in both parameters depends on the interacting components of strain and electric fields.

The presence of non-degenerate spin sub-levels in the ground state is the reason for the presence of Zero-Field Splitting (ZFS) D_{gs} . The non-degeneracy or a lift in degeneracy occurs due to the symmetry of the defect. The presence of an odd species such as Nitrogen in the lattice deforms the overall lattice structure to adopt C_{3v} symmetry. Therefore, the ZFS between the $m=0$ and $m=\pm 1$ states arise as a result of deformation in the molecular orbitals of the unpaired electrons.

As shown in Fig. 2.2, the presence of a radiative transition from the excited triplet state to the $m=0$ ground state manifold contributes to the fluorescence via the optical spectra. The other manifolds such as $m=\pm 1$ have inter-system crossings through non-radiative decay mechanism to populate the $m=0$ manifold of the ground state. The Optically Detected Magnetic Resonance (ODMR)[46] is a double resonance technique. As exciting the NV^- centers with far-off resonance radiation populates the $m=0$ sub-level, tuning microwave frequency across D_{gs} enables population transfer to $m=\pm 1$ state. A reduction in the overall fluorescence is observed, which differentiates the bright ($m=0$) and dark ($m=\pm 1$) states. The resonance occurring at the zero-field splitting frequency is taken as a fingerprint ODMR spectra that ensures the presence of NV^- . The contrast of the spectra that corresponds to the difference in bright and dark state depend on the number of NV^- centers present and their interaction probability with the applied microwave field. With ODMR spectra, quantum sensing protocols and simulations such as Rabi oscillations, can be performed over the addressed two-level quantum systems.

As shown in magnified section of Fig. 2.2, the ZFS at ideal condition with C_{3v} symmetry as shown in Fig. 2.3b, at room temperature and without any other interactions from the environment is ~ 2.87 GHz. In real environment, as shown in Fig. 2.3c, due to the presence of different bond length in case of C-N and C-C breaks the symmetry[47]. The deformation of molecular orbital due to the symmetry breaking, lifts the degeneracy in the $m=\pm 1$ states. This symmetry breaking gives two resonance across the ZFS corresponding to each spin manifolds. This E-Parameter under no externally applied field case, changes for different crystals as the amount of local strain varies due to various factors. In the presence of external magnetic field, the degeneracy in dark states lifts as a function of magnetic field strength. As a consequence, the split or E-parameter varies symmetrically across the ZFS frequency in the ODMR spectra.

Due to interactions from Electric and strain fields, there will be a shift in D-Parameter as well as in E-Parameter according to the axial and non-axial coupling coefficients of those interactions. In case of increase in temperature, a shift in D-parameter is observed[19], whereas the E-parameter remains decoupled to the interaction. By taking account of the consequences in the observed ODMR spectra due to stray fields, the chosen NV^- centers can be used to quantify the perturbations due to the externally applied fields such as magnetic, electric and strain fields.

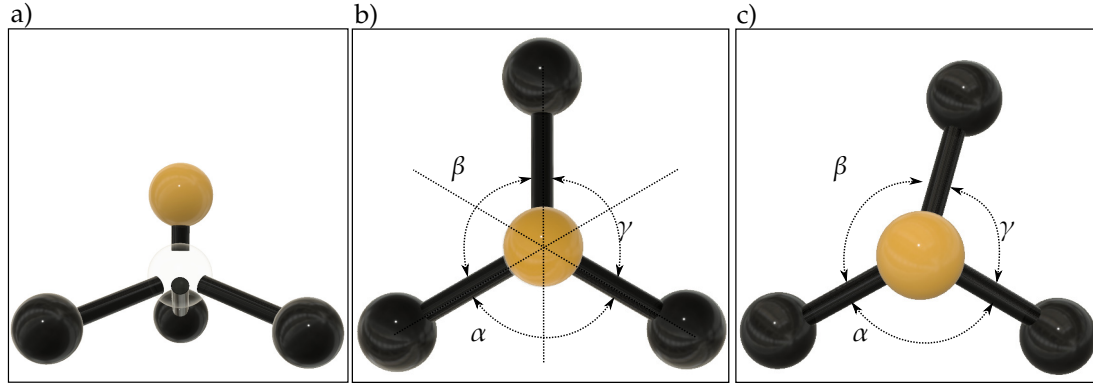


Figure 2.3: C_{3v} symmetry in lateral and top views. The Nitrogen-Vacancy site along with neighboring carbon atoms, define the point defect symmetry to be C_{3v} . a) represents the lateral view of the point defect. The presence of nitrogen atom (Yellow) near vacancy site with nearby carbon atoms (Black). This symmetry contributes to the deformation of molecular orbital, becomes a reason for the occurrence of ZFS. b) shows the top view of the point defect, it satisfies the character table of the C_{3v} symmetry group. The planes(dotted lines) show the mirror symmetry, and the α , β , γ are equal to 120° . In presence of different bond length between C-N, C-C near the defect breaks the symmetry as shown in c). This deformation lifts the degeneracy between $m=\pm 1$ manifold in ground state of NV^- .

2.2 Experimental Set-up

In this section, we introduce the experimental set-up and various components along with its working principles.

An overall experimental set-up as shown in Fig. 2.4, is an assembled workbench. It comprises of a fibre coupled diode laser⁴, an assembled confocal microscopy, a co-planar waveguide (CPW)[48], a Photon Multiplier tube, a CCD Grating Spectrometer⁵, a CMOS Camera⁶, a Data Acquisition System⁷ works with ARTIQ Programming platform and a Frequency Quadrupling Circuit.

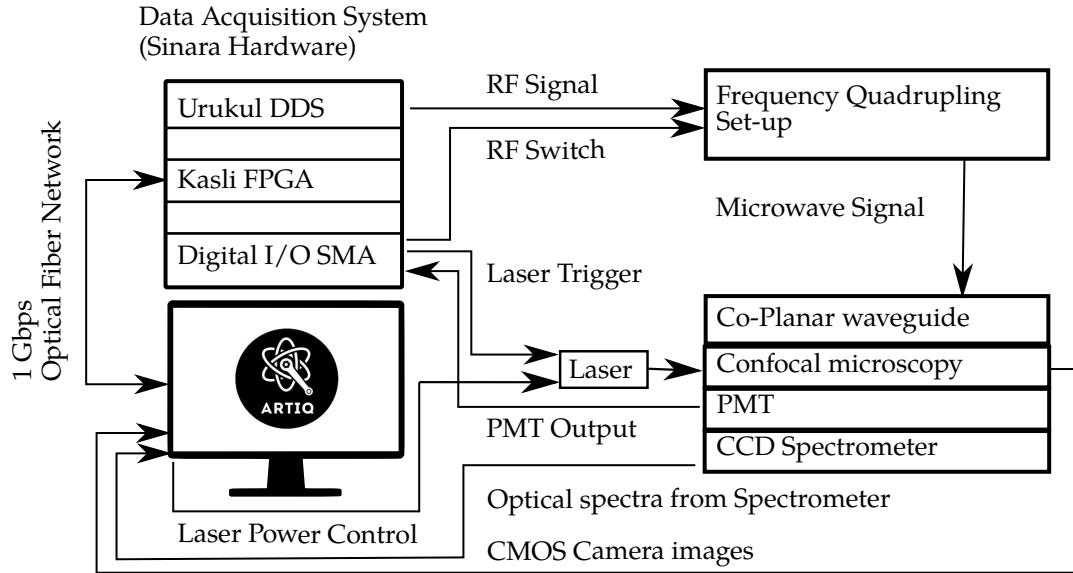


Figure 2.4: **Overall Experimental set-up.** The arrows are to show the uni- and bi-directional communication establishments in the Experimental Set-up. An optical network connection with 1 Gbps bandwidth is established between the Host PC and the DAQ for faster communications. Two peripherals, Urukul DDS and Digital I/O SMA are connected to Kasli (FPGA) via 30 pin IDC connectors (Eurocard Extension Module). RF signals from the Urukul DDS are quadrupled and transmitted using CPW. The fiber coupled laser is triggered by a TTL signal from Digital I/O SMA peripheral and the output power control is handled via the Host PC. The resulting images and the emitted spectra of a diamond from the confocal microscopy is acquired using the CMOS Camera and the CCD spectrometer respectively. The PMT TTL outputs during experimental events are recorded using the input ports of Digital I/O SMA peripheral. The data and the set parameters are stored in the form of datasets with the help of ARTIQ Programming Platform.

2.2.1 Data acquisition system(ARTIQ) and Microwave transmission

The Data acquisition(DAQ) system consists of a Field Programmable Gate Array (FPGA) called Kasli, along with Digital I//O SMA (DIO) and Urukul DDS⁸ peripherals. As shown in Fig. 2.5, the kasli board is used as a master controller of the DAQ. An optical fibre based network connection from SFP0⁹, with 1 Gbps bandwidth is established with the host PC. It is capable of controlling 12 peripherals simultaneously via EEM (Eurocard extension module connectors) with a timing resolution of 1 ns. The DIO has 4 output SMA ports, capable of producing TTL pulses with minimum width of 3 ns and with maximum toggle rate of 150 MHz at 50 % duty cycle. It also has 4 input SMA ports, capable of counting TTL events on demand. The Urukul DDS with AD9910 chip, is capable of producing 0-400 MHz RF signal with a resolution of 0.23 Hz (32-bit). It is interfaced via two EEM connectors to enable simultaneous control over RF

⁴Toptica iBeam Smart

⁵Thorlabs CCS175 CCD Spectrometer

⁶Thorlabs CMOS Camera

⁷Based on Sinara hardware

⁸Direct Digital Syntheser

⁹Small form-factor pluggable

output frequency, phase and switching. It is operated with its default clock frequency of 1 GHz and other options includes controlling clock frequency using external SMA connector or using MMCX on-board connector that gets clock reference from the Kasli board.

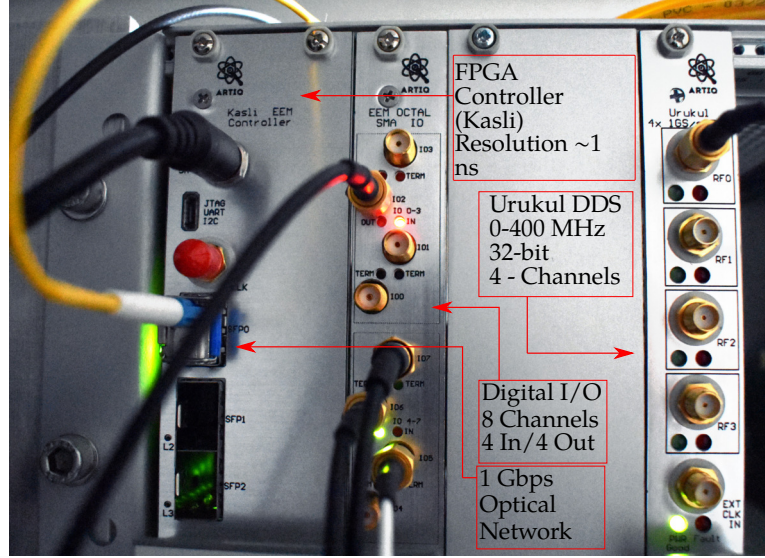


Figure 2.5: **Data Acquisition(DAQ) System.** In the image, the module on the left belongs to the Kasli controller board with three SFP interfaces in front. One of them connected to an optical fibre network to establish 1 Gbps connectivity with the Host PC. Next to the Kasli board is the Digital I/O SMA peripheral with 8 SMA ports. First four from top, belongs to TTL Inputs, can count TTL pulses on demand, as specified by the python code which is executed from ARTIQ platform. Next four SMA ports, belong to TTL Outputs, capable to produce TTL pulses with minimum width of 3 ns and maximum toggle rate of 150 MHz. Next to the Digital I/O, is the Urukul DDS based on AD9910 Chip, interfaced to kasli via two EEM connectors for simultaneous RF output and switching. First four SMA ports from the top, belong to RF output channels. The last SMA port is for external Clock reference control.

The Advanced Real-Time Infrastructure for Quantum physics (ARTIQ) is an open source high-level programming language based on python. With the help of ARTIQ installed in the host PC, the DAQ system is controlled over network with a Graphical User Interface and an experiment scheduling system. Using this platform, time-critical experiments are described in a python code. They are compiled and executed on the FPGA with a nano-second timing resolution. Using the Remote Call Procedure (RPC) protocol, the FPGA is interfaced with the python code on the Host PC and the data is acquired at sub-microsecond latency. The non-realtime python code is executed in the ARTIQ Environment for manipulating and analyzing data that are acquired from the FPGA. All the data and parameters of an experiment executed, are stored as a dataset¹⁰ in the host PC.

We require a switchable, frequency tunable microwave source in the experiment set-up¹¹ along with a control over the signal power. The DDS peripheral is capable of producing RF signal in the range of 0-400 MHz, on command using ARTIQ. Since the DDS works with 1 GHz clock frequency, a mirror signal¹² with respect to the clock frequency is transmitted along with the demanded frequency. The frequency quadrupling circuit(FQC) is assembled as shown in Fig. 2.8 to quadruple the RF frequency to generate microwave signals.

¹⁰HDF5 dataset file

¹¹ODMR spectra

¹²Set ~300 MHz, Mirror signal (1 GHz - 300 MHz)= 700 MHz

Coplanar waveguide(CPW)

The CPW as shown in Fig. 2.6, is used in the experiment to transmit the quadrupled RF signal from the FQC. It has a wideband transmission with zero-cutoff frequency. As shown in the design, the ground and the conducting metal are fabricated in the same plane over the dielectric material. Accordingly, the width of the conducting material and the dielectric region between the conducting and ground plane are of 1.5 mm and 0.25 mm respectively. The field lines of the transmitted microwave signal, reaches the ground plane by air as well as dielectric region. This operating mode called Quasi-TEM mode which involves transmission in two different mediums with two different group velocities. The Quasi-TEM mode is close to TEM mode, as the fields are zero in the direction of propagation. In the experiment, it is used as a substrate for micro-diamonds which increases the probability of microwave interaction with the NV^- centers¹³.

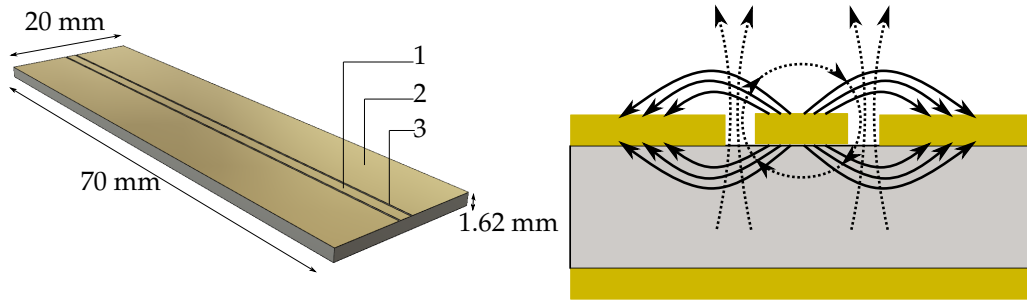


Figure 2.6: **Coplanar waveguide Design and its Working.** On the left, a rendered model of the coplanar waveguide is displayed. The conducting strip(1) and the ground plane(2) is fabricated on top of the dielectric material. The width of the conducting strip and the dielectric region(3) between the conducting and ground plane, are 1.51 mm and 0.25 mm respectively. On the right, the image represents the working of CPW. The solid lines represent the electric field distribution and the dashed line represents the magnetic field distribution. The field lines propagates through air and dielectric, the modes are called as Quasi Transverse Electromagnetic Mode(TEM). The electric and magnetic field components are zero in the direction of propagation.

¹³ODMR and related techniques

2.2.2 Confocal Imaging

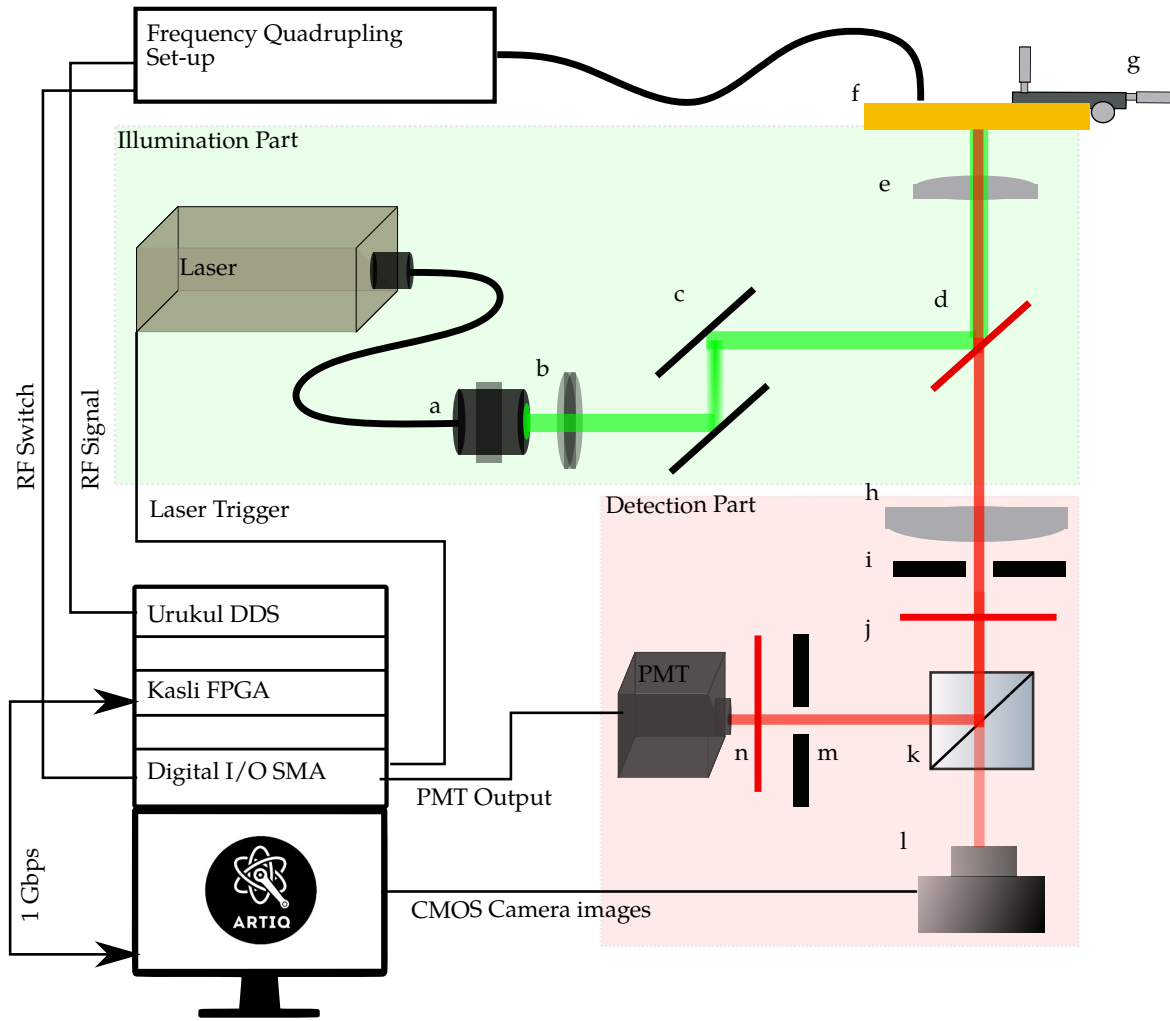


Figure 2.7: Schematic overview of the confocal microscopy along with other components. An output coupler (a), gets input fibre from the laser and emits collimated beam with beam diameter of around 1 mm. A quarter waveplate (b) is used to generate circularly polarized light. Couple of adjustable mirrors (c) are used for spacial positioning of the laser beam. Longpass dichroic mirror (d) of cut-off 550 nm, reflects excitation laser light of 519(1) nm and transmits fluorescence light which is above 550 nm. An aspherical lens (e) with short focus of 10 mm, is used as an objective lens to focus and collect, the excitation laser beam and the fluorescence light respectively. A CPW (f) is used as a substrate for the micro-diamonds and to transmit microwave signal near proximity to the NV⁻ centers. A XYZ stage (g) is used to adjust the position of the CPW with micrometer resolution. A Collecting lens (h) of $f=150$ mm is used to focus the collected light onto the image capturing and photon counting systems. An aperture (i) is placed to block stray light and helps in aligning the light beam. A Long pass optical filter (j) of wavelength 600 nm, is to block the excess excitation laser light and co-propagating stray light. A non-polarizing beam splitter (k) of ratio 90:10 is placed in the beam path, 90 percent gets reflected and 10 percent gets transmitted. A CMOS Camera (l) is placed behind the beam splitter to capture images of the diamonds and helps in marking the position of the diamond with respect to the lab frame. On the reflecting side of the beam splitter, another aperture (m) and longpass filter (n) are placed to block non-paraxial and stray light, to enhance the contrast of the light entering PMT. The solid black lines represents the connection establishments for controlling and data transfer as shown in Fig.2.4.

The confocal microscopy is assembled using various discrete optical components¹⁴. We require an optical microscopy to locate and spatially resolve NV⁻ centers in the micro-diamonds. As shown in Fig 2.7, the microscopy works on the basis of fluorescence imaging technique. Using a dichroic longpass mirror in the set-up, attenuates the illumination laser light on the image plane. Hence the overall contrast of the acquired images, is enhanced compared to conventional 4f imaging technique. As the illumination light and the reflected fluorescence light, traces through the same objective lens, leads to a convolution of two Point Spread Functions (PSF). Compared to the PSF of the conventional 4f optics, the confocal PSF has a reduced FWHM which leads to a better resolution. The collection efficiency of the optics is determined by the numerical aperture of the objective lens used. The fluorescence emission of the micro-diamonds is isotropic and only a fraction of about ~10% is collected by the imaging optics. Hence, this unidirectional collection efficiency bottlenecks the set-up to address NV⁻ centers that emit in other directions.

The fibre-coupled laser with wavelength 519(5) nm is coupled to an output coupler. The laser output is triggered and the power control is established using the host PC via serial I/O. The output laser beam from the coupler, is passed through a quarter waveplate to produce circularly polarized light. The polarized light is to address NV centers oriented isotropically in the lattice structure. Using an adjustable pair of mirrors, the collimated laser beam is spatially positioned. A longpass dichroic mirror with a cut-off wavelength of 550 nm, is positioned at ~45° in between two lens system. The collimated laser beam is reflected by the dichroic mirror onto the objective lens. The objective lens with high NA, focuses the laser beam onto the micro-diamonds placed on the conducting strip of the CPW. The fluorescence light from the NV⁻, is collected by the objective lens and the co-propagating, reflected excitation laser beam is attenuated by the dichroic mirror. The fluorescence light above 550 nm is transmitted and the spectra depends on the transmission characteristics of the dichroic mirror. A collecting lens of f=150 mm is placed behind the dichroic mirror in the beam path to focus the collected fluorescence light. Followed by a pair of an aperture and longpass optical filter with cutoff of about 600 nm. This pair is to block stray light and to attenuate excess excitation laser light in the optical beam. A non-polarizing 90:10 beam splitter is placed in the beam path which reflects 90 % of the obtained light and the rest gets transmitted to reach the CMOS camera. On the reflecting side of the beam splitter, a PMT is placed behind the pair of aperture and longpass filter to block stray light and to enhance the sensitivity of photon counting events. For obtaining the optical spectra of NV⁻ centers, the grating CCD spectrometer is used on the reflecting side of the beam splitter.

¹⁴Thorlabs Components

2.3 Calibration

In this section, the working principles and the calibration of various discrete functional sections in the experimental set-up are reported.

2.3.1 Frequency Quadrupling Circuit

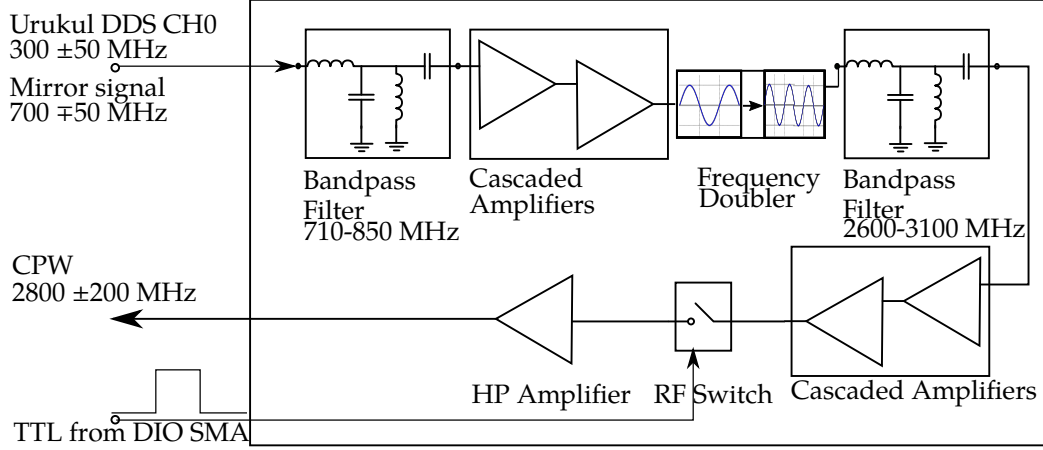


Figure 2.8: **Schematic of the Frequency Quadrupling Circuit.** The RF signal in the range of 300 ± 50 along with the mirror signal 700 ± 50 MHz from the DDS, are fed into the circuit. Signals other than mirror signals are filtered out by the bandpass filter. Followed by a cascaded amplifier with gain ~ 30 dB. After the frequency doubler, the transmitted signals contains attenuated 4th harmonics. The procedure is repeated using a bandpass filter in the range of 2600-3100 MHz, to selectively transmit quadrupled signals. Followed by amplification of the 4th Harmonics with another cascaded amplifier pair. The amplified microwave signal output is controlled using a additional high isolation RF-switch triggered using DIO, to account for delays during the quadrupling process. The switchable microwave signal is amplified further using a high power amplifier with a gain of 45 dB. The amplified signal is transmitted using the co-planar waveguide.

Figure 2.8 shows a schematic working representation of the frequency quadrupling circuit which is used along with the DAQ and ARTIQ for the microwave generation. Figure 2.9a, represents the plot of frequency response of the output signal from the Urukul DDS, acquired with a spectrum analyser. The corresponding mirror signal that propagates along with the demanded signal, is chosen for quadrupling, to generate the microwave signal in the range of 2800 ± 200 MHz. Using a bandpass filter¹⁵ with a passband range of 710-850 MHz, mirror signal is filtered and transmitted. Subsequently, a cascaded amplifier¹⁶ with a gain of ~ 30 dB, is used to amplify the signal. Followed by a frequency doubler¹⁷, which doubles the frequency of the input signal. Along with the frequency doubled signal, the transmitted spectra has a quadrupled harmonics in the microwave regime. By using a bandpass filter with passband in the range of 2600-3100 MHz, the quadrupled signal is selectively transmitted. Further, it is amplified using another cascaded amplifier pair of same configuration. Figure 2.9b, shows the frequency response of the quadrupled signal in the range of 2.6 to 3.0 GHz. We require microwave signals for time-critical experiments that are executed from FPGA. An additional switching control over the microwave signal is established with a high isolation RF-Switch¹⁸ along with inherent RF switching capability of the Urukul DDS. This additional RF switch is controlled via the described python code with the Digital I/O peripheral. As shown in Fig. 2.10a, a delay of 50 ns is introduced between the DDS RF switch and the high isolation switch to clip the rise time artifacts in the RF signal. This coupled switches are helpful as a time flag to differentiate different frequencies and its interaction times in the experiments. A high-power RF amplifier¹⁹ is used to amplify the microwave signal with a gain of ~ 45 dB. Figure 2.10b)

¹⁵VBFZ-780-S+

¹⁶ZX60-3018G+ and ZX60-8008E-S+

¹⁷FX3000+

¹⁸ZASW-2-50DR+

¹⁹ZHL-16W-43+

shows the amplified microwave signal, which is transmitted through the coplanar waveguide for experiments.

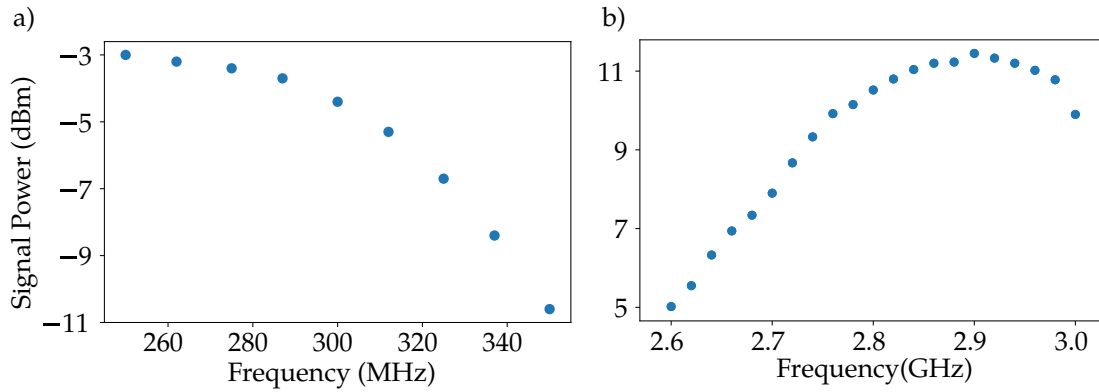


Figure 2.9: **Frequency response of the signals, before and after Quadrupling circuit.** a) shows the frequency response of the DDS output (errorbars are smaller than the datapoints) which is measured with a spectrum analyser. The input attenuation and the phase of the signal are set to 0 dB and 0° respectively, using the ARTIQ platform. The plot shows a non-linear frequency response over the range of 250-350 MHz. b) shows the frequency response of the output quadrupled signal after the second cascaded amplifier. On observation, we find the response to have a reversed non-linear response, comparing with the DDS output due to use of mirror signals for quadrupling. On measuring the reference power of the output signal, we estimate the circuit to have a gain of ~ 18 dB till the cascaded amplifier.

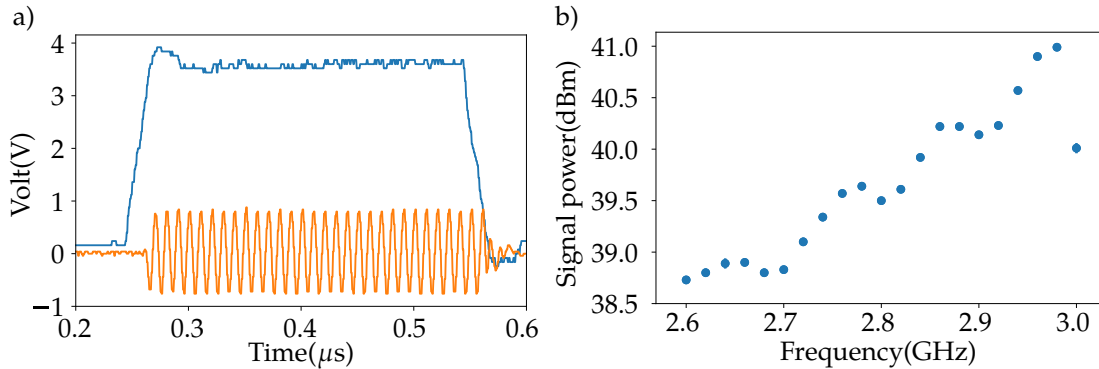


Figure 2.10: **Delay rectification with the high isolation RF-Switch and the frequency response of high power amplifier.** a) shows the RF trigger TTL signal (Blue) along with the RF output (Orange) from the high isolation switch. Using an oscilloscope with inputs shorted to 50 Ohm, the TTL trigger for switching high isolation RF switch and the DDS output are analysed. By introducing a delay of ~ 50 ns between the two triggers, the rise time delays in DDS output is avoided. b) represents the frequency response of the microwave signals (errorbars are smaller than the datapoints) output from the high-power amplifier. An attenuator of 10 dB is connected at the input of the high power amplifier, the amplified output is connected to the spectrum analyser with the help of high-power 33 dB attenuator with attached heat sink. The response plotted shows an overall gain of ~ 50 dB from the output of DDS. Subsequently, the amplified signal is connected to the co-planar waveguide for transmission.

2.3.2 Diode Laser and Digital Modulation

The fibre coupled diode laser²⁰ shown in Fig 2.11a, is used as a laser source in the experimental set-up. This diode laser emits at a wavelength of 519(5) nm and the corresponding output power can be controlled using the host PC through a serial connection(Fig. 2.11b). The laser output can be externally modulated using analog or digital inputs at a maximum rate of 250 MHz via SMB connectors. The diode laser output is coupled into an optical fibre using a docking accessory²¹, where the coupling efficiency can be optimized.

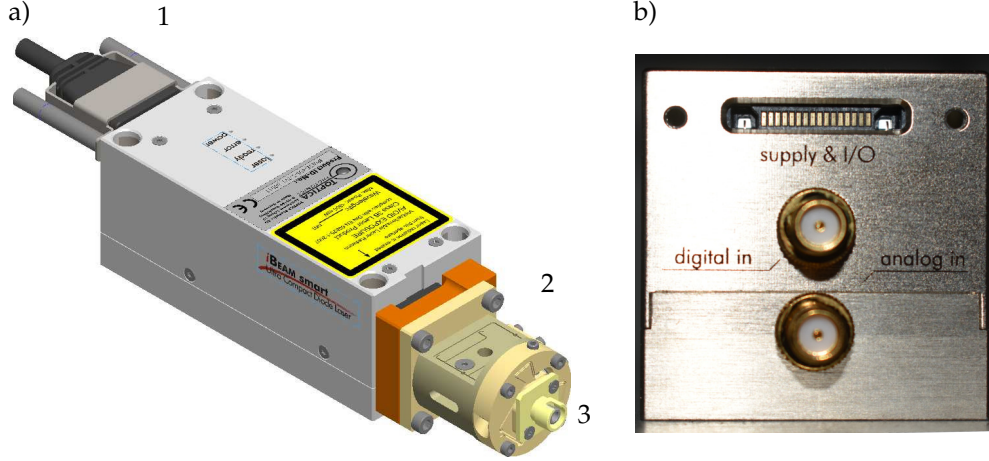


Figure 2.11: **Model of a fibre coupled diode laser and its connectors.** a) CAD model of the fibre coupled laser with a serial connection(1). The laser output is optimised through the docking accessory(2) and an optical fibre is connected at the fibre coupler(3). The CAD model sketch is taken from the technical drawings[49]. b) shows the back panel of the laser module with a serial I/O for PC connection. Two SMB connectors are for digital and analog modulation control respectively.

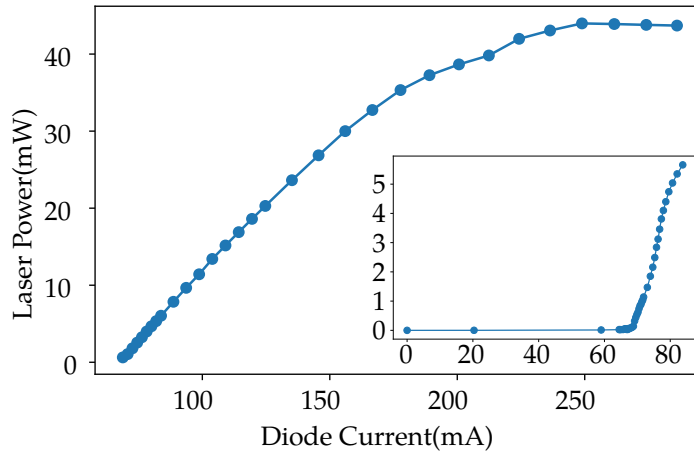


Figure 2.12: **Output power characterization of the fibre coupled diode laser.** Laser power is measured using a power meter, as a function of an input diode current. The errorbars are smaller than the data points. The inset graph data corresponds to the lower diode current region, shows that the laser output starts at the threshold diode current ~ 67 mA. The laser response in the higher diode current, is linear until around ~ 180 mA and saturates towards maximum diode current. The maximum possible laser output power is measured to be ~ 43 mW.

The beam from the optical fiber is collimated with a beam waist of ~ 1 mm. The calibration of the laser power is necessary to understand the response with respect to the input diode current.

²⁰Toptica iBeam smart

²¹iBeam smart dock

As a function of varied diode current which is controlled using the host PC, the output power is measured. Figure 2.12 shows the characterization plot of the laser response with respect to the diode current. The inset graph data²², shows that the calibration at lower diode current region where the lasing action starts at a threshold diode current of approximately ~ 67 mA is in agreement with the data sheet from the manufacturer. The output characteristics at higher diode current²³ shows a linear output response until around ~ 180 mA and starts saturating beyond that limit, reaching the maximum power of around ~ 43 mW. From the characterization data, the laser power at particular laser settings from the host PC is known. The fibre coupling has to be optimized regularly to keep the coupling efficiency at maximum.

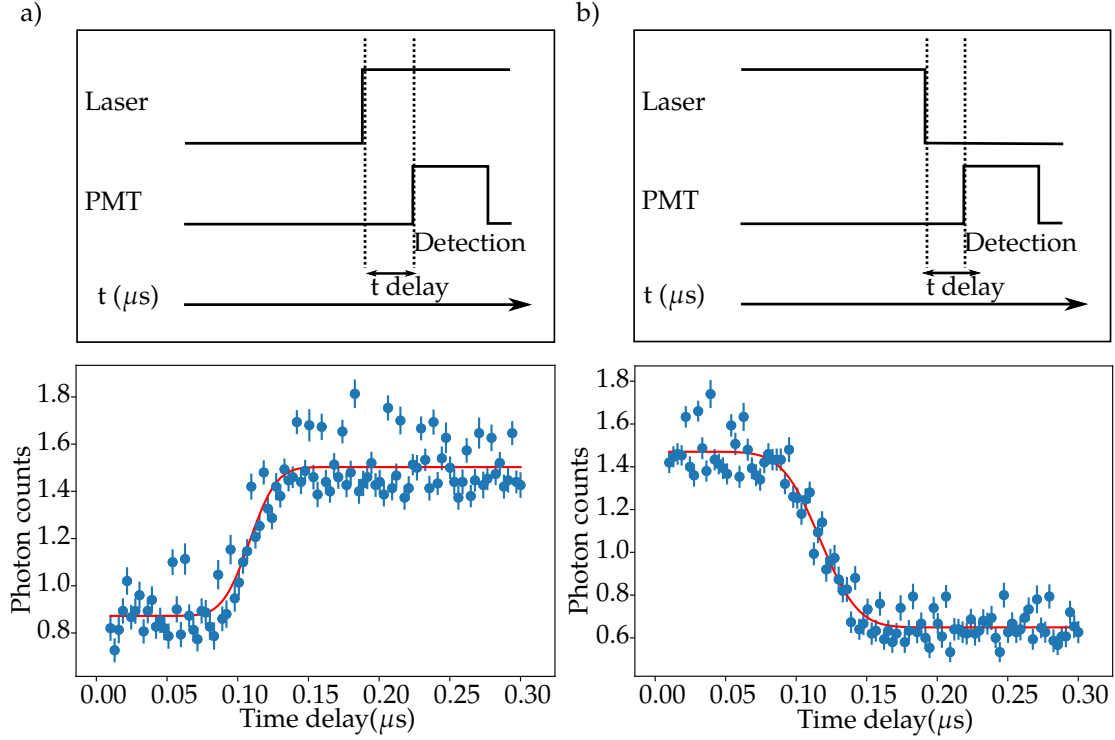


Figure 2.13: **Experimental sequences and estimation of delays in triggering laser output.** a) To analyze the delay involved in digitally modulating the laser output, a delay between triggering laser output and the PMT detection window is varied. The corresponding fluorescence data (blue data points) from the NV as a function of varying delay is plotted. Similarly, b) shows the experimental sequence described to analyze fall time response of the laser modulation. Using a composite model of step function and Gaussian over the data, we extract the average rise time (0-90 %) and fall time (100-10 %) to be $0.13(1) \mu s$.

In the experiments, the time critical experimental code involves digital modulation of the laser output. The laser output is triggered via the TTL pulse from Digital I/O peripheral. The rise time of the diode laser in case of digital modulation is mentioned to be about ~ 1 ns. The estimation of delay involved in laser modulation is carried out using the fluorescence light from the NV center. The PMT is used to measure the fluorescence output in specified time window, as described in the kernel python code. As shown in Fig. 2.13, the experimental sequence is designed to measure fluorescence light as a function of change in delay between laser positive trigger and the detection time window. Similarly the experimental sequence is modified to measure the same during a negative trigger. Using a composite fit of Gaussian and step function over the data, we extract and average the rise/fall time to be about $0.13(1) \mu s$. Hence, a minimum delay of ~ 130 ns is introduced into the code as a constant to reduce the systematic uncertainty in the photon count during time critical operations.

²²Measured using Fieldmate VIS sensor, due to its higher resolution in low power regime

²³Measured using Thorlabs PT160T power meter

2.3.3 Imaging optics

The confocal segment in the experimental set-up, is a modified 4f imaging optics. Figure 2.14a, shows the working principle of the microscope. The objective lens at a distance of focus from the object plane, collects the light emitted with its high numerical aperture. The object information is Fourier transformed and collimated by the objective lens at the focus, in the direction of light propagation. The dichroic mirror filtered object information from the backplane, is collected by the collection lens of higher focus. The collected object information is focused at the image plane. The lateral magnification of the 4f imaging optics is the ratio of focusing length of collecting lens to the focusing length of the objective lens.

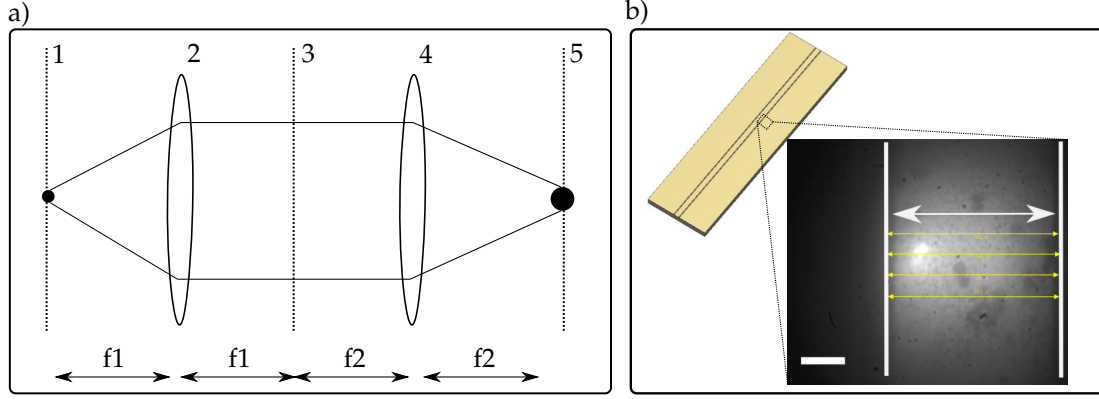


Figure 2.14: **Working principle of a 4f imaging system and the magnified image of the dielectric section of the CPW.** a) The object information from the object plane(1) is collected by objective lens(2) placed at the focus f_1 . The light gets collimated, the image from the Fourier plane(3) is collected by a collective lens(4) of longer focus kept at f_2 . It is focused onto the image plane at the focus f_2 . The image shown in b) represents the dielectric part of the co-planar waveguide magnified using the 4f imaging optics and captured by the CMOS Camera at the image plane. Scalebar(white) in the left corner, corresponds to 200 pixels. Two white bars represent the end of the dielectric region and the white line with arrow marker represents a width of 785(5) pixels. From the pixel length and the real length of the dielectric region(~ 0.25 mm), we extract the magnification and resolution of the optics to be about 16X and $\sim 0.3 \mu\text{m}/\text{Pixel}$ respectively.

To determine the lateral magnification of the confocal microscopy in the experimental set-up, a part of the co-planar waveguide is imaged. As shown in Fig. 2.14b, the dielectric region of width 0.25 mm, is imaged using 4f lens system which consists of 10 mm objective lens and 150 mm collecting lens with dichroic mirror in between²⁴. The image is captured using the CMOS Camera²⁵ with a pixel size of $5.2 \mu\text{m}$. The width of the dielectric structure is measured to be about 785(5) in pixels. From the measured data, the magnification of the imaging optics and the resolution are calculated to be about $\sim 16\times$ and $\sim 0.3 \mu\text{m}/\text{Pixel}$ respectively.

As shown in Fig. 2.15a, the laser beam is directed onto the micro-diamond lying on the CPW surface. Using the micro-meter screws of the XYZ stage, the CPW is adjusted to get a focused image of the micro-diamond. Figure 2.15b) shows the captured fluorescence image of the micro-diamond which is in random and asymmetric shape. The exposure settings of the camera is adjusted to get an unsaturated image. As shown in Fig. 2.16, the averaged intensity profile across the XY coordinates with respect to the camera frame is plotted. Using a two Gaussian composite model fit, we extract the widths of two Gaussian along two axes to be about 13.2(3), 16.8(3) and 14.1(4), 17.8(4) pixels respectively. Using the resolution of the imaging optics $\sim 0.3 \mu\text{m}/\text{Pixel}$, the FWHM of the overall diamond size is calculated. Hence, the mean size of the diamond along X and Y axis is deduced to be about 21.2(4) μm and 22.5(6) μm . Estimating the beam waist using this fit is insignificant, due to the inhomogeneous cluster size of the NV centers addressed in the diamond. Hence, the beam waist of the confocal set-up is assumed to be smaller ($< 5 \mu\text{m}$) compared to the size of the diamond, based on the observations. The mean size of the diamond is also an approximate estimation, due to the lack

²⁴Fluorescence imaging

²⁵Thorlabs CMOS Camera

of information of the size of the diamond in Z-direction (Axis point out of the paper) as well as the inhomogeneous distribution of defects reduces the accuracy of this estimation.

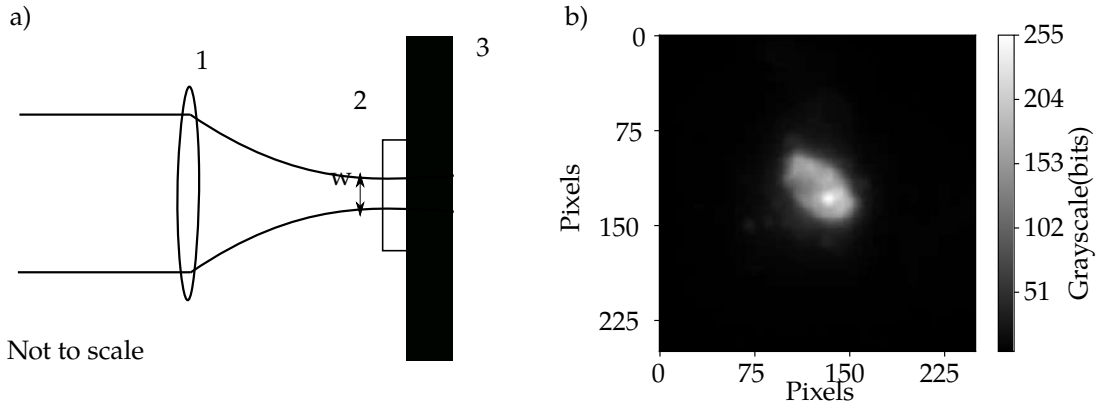


Figure 2.15: **Beam waist estimation of the imaging system** a) Schematic of the focusing beam with a Gaussian profile. Collimated beam is focused by the objective lens(1) on to a micro-diamond(2) placed on the co-planar waveguide(3). b) shows the corresponding image of the diamond with laser beam on it. Image settings of the CMOS camera are altered to get unsaturated image, ROI of the image is selected as 250x250 pixels. The vertical calibration bar represents the intensity with gray-scale values in bits.

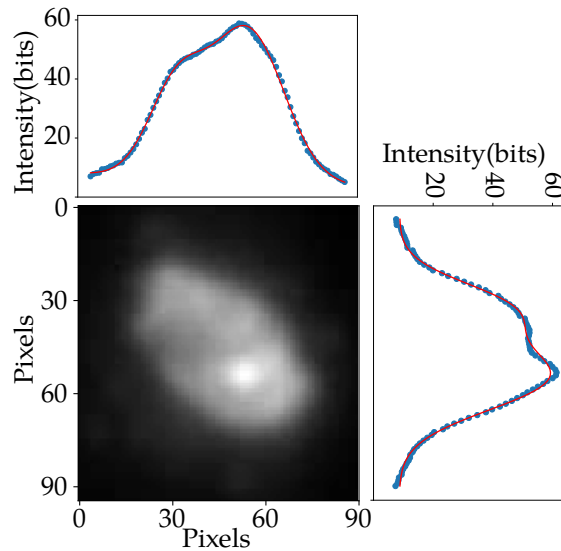


Figure 2.16: **Intensity profile of the image across XY frame.** Using the CMOS Monochrome camera, a image of the micro-diamond is captured. A Region of Interest(ROI) of 90x95 pixels is chosen, that shows the captured image. The mean size across the XY coordinate is measured by taking mean intensity profile with respect to the plane. Using a composite two Gaussian fit model, we extract the widths of these Gaussians along two axis to be about 13.2(3),16.8(3) and 14.1(4), 17.8(4) pixels respectively. The mean cross-section of this diamond(FWHM) is estimated to be about 21.2(4) μm and 22.5(6) μm .

2.3.4 Spectrometer

The Grating Spectrometer²⁶ works in the range of 500-1000 nm with sub-nanometer precision. Figure 2.17 shows its working principle. The light that couples into the device, is resolved into its spectral components as a result of diffraction due to the grating. The spatially resolved spectrum is recorded with the CCD. The resolution of this spectrometer depends on the grating constant and the pixel density of the CCD Array²⁷. The accuracy of the device varies as a result of incidence angle of light in the horizontal plane (XY Plane).

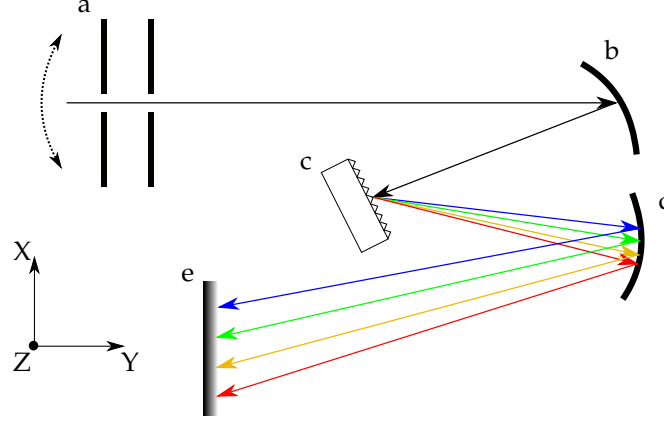


Figure 2.17: **Working principle(Not to scale) of the grating spectrometer.** A grating spectrometer configuration known as Czerny Turner design[50] is adapted. a) Input port to couple light into the spectrometer, b) a reflecting concave mirror to focus the incident light, c) a grating that diffracts and resolves the spectra, d) Another reflecting concave mirror to focus the resolved spectra e) CCD to detect the spatially resolved spectra.

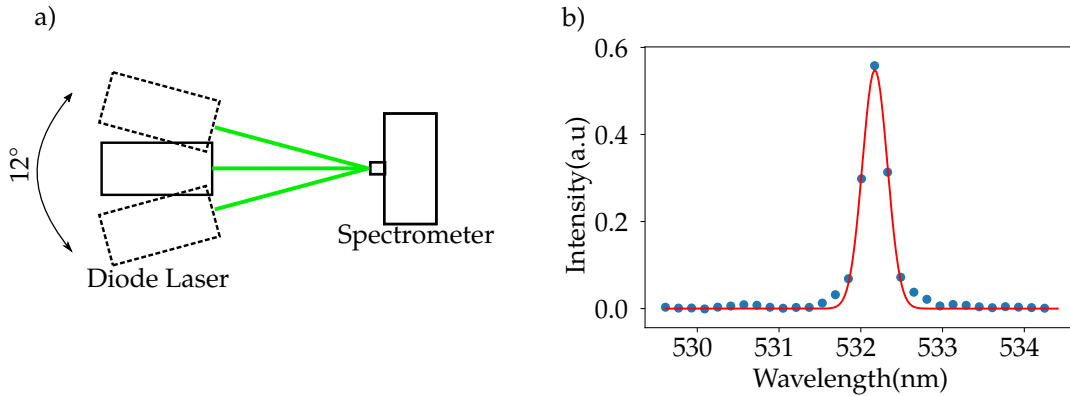


Figure 2.18: **Experimental procedure for calibration of systematic shifts.** a) Schematic of a set-up (Not to scale) that has been used. The incidence angle of the laser beam with a wavelength ~ 532 nm, is changed over a range of $0-12^\circ$ with an uncertainty of 2° and corresponding spectra are recorded. b) The plot represents averaged spectra of laser at 9° relative to the first position. Using a Gaussian model fit over the spectra, we extract observable parameters of the spectra such as FWHM, center position and amplitude to be $0.216(5)$ nm, $532.172(3)$ nm and $0.55(1)$ respectively.

To determine the systematic shifts in spectra, a diode laser of wavelength 532 nm is used. As shown in Fig. 2.18a, the incident angle of the beam at the coupling port is varied and the corresponding spectra are recorded. Figure 2.18b, shows a data representing the spectra of the laser beam at 9° with respect to the first position. Using a Gaussian model over the spectra, we extract the free parameters such as width, center position and amplitude are extracted with uncertainty bounds to be $0.216(5)$ nm, $532.172(3)$ nm and $0.55(1)$ respectively. As shown in Fig. 2.19a, the shifts in center position with respect to the incident angle is plotted. Using a linear model over the response, we extract the slope to be $0.12(1)$ nm/ $^\circ$ change in the incident angle.

²⁶Thorlabs CCS175 CCD Spectrometer

²⁷3648 Pixel CCD Line Array

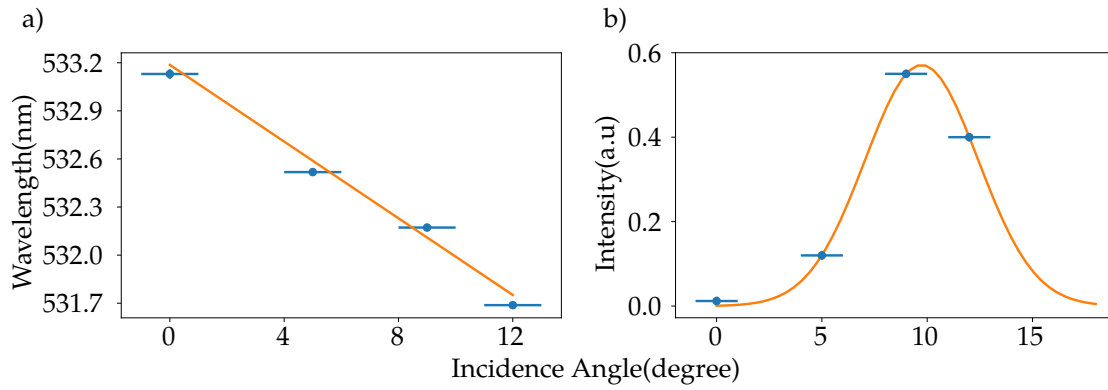


Figure 2.19: Calibration of the systematic shift due to varied incident angle at fibre coupling port of the spectrometer. a) As a function of varied incident angle at the coupling port of the spectrometer, a shift in wavelength of the incident laser light is noticed. Errorbars in incidence angle (x-axis) belongs to uncertainty in deducing the angle of laser position and errorbars in wavelength data (y-axis) belongs to the width extracted using Gaussian model. By using a linear model over the data, we extracted the slope of the response to be 0.12(1) nm per degree change in the incident angle. b) The plot shows the change in intensity(errorbars are smaller than the datapoints) of the spectra with respect to corresponding angle. Using a Gaussian model over this response, we extracted the width of $\sim 4^\circ$ which corresponds to 0.48(1) nm shift in spectra.

Figure 2.19b) shows the intensity variation of the shifting spectra with respect to the incident angle. Using a Gaussian model fit on the data, we get a FWHM²⁸ of the intensity data to be $\sim 4^\circ$ which corresponds to 0.48(1) nm. Hence, optimizing the incidence angle to acquire maximum intensity, reduces the systematic uncertainty of the spectrometer to ~ 0.5 nm. A line CCD array is used in the spectrometer, hence a change in the incident angle in the vertical direction (YZ plane) will not significantly affect the accuracy of the spectrometer, rather it affects the intensity measured.

²⁸Full Width Half Maxima of the Gaussian model used

2.3.5 Magnetic Field

We require a static, tunable, homogeneous magnetic field near the micro-diamonds²⁹. A permanent cylindrical shaped magnet³⁰ with a remanent magnetization of 1~1.3 Tesla, is chosen to provide the required magnetic field. As shown in Fig. 2.20, the tunability of the magnetic field strength and the desired vector directions are ensured by moving and positioning the magnet with respect to the region of interest. As shown in Fig. 2.21a, the calibration of magnetic field strength of the permanent magnet as a function of distance in the axial direction, is carried out using a hall probe³¹. Figure 2.23, shows the plot (Blue data points) of recorded magnetic field in the axial direction using the hall probe³². Using a fit model of $\frac{1}{x^2}$ that represents the dipole response of the magnet, we deduce the coefficient of the function to be about 259(2) G/cm². Due to the dipole response of the permanent magnet, the field across the zone of interest is inhomogeneous with an unknown resultant vector direction. Figure 2.21b) shows the vector plot of the simulated dipole magnet with the magnetization same as the permanent magnet. From the simulation, the magnetic field strength contribution due to inhomogeneous fields near the region of interest (Black dotted circle) in Fig. 2.20 is acquired. In the Fig. 2.23, the gray shaded region represents the simulated data that includes uncertainty budget due to inhomogeneous field strength in the sphere zone where the micro-diamonds reside during the experiments. The measured data using the hall probe is found to have a systematic shift from the simulated data. Figure 2.23 shows a residual plot with a magnified plot to showcase the uncertainties in the case of lower magnetic fields along with the systematic shift in the measured and simulated data.

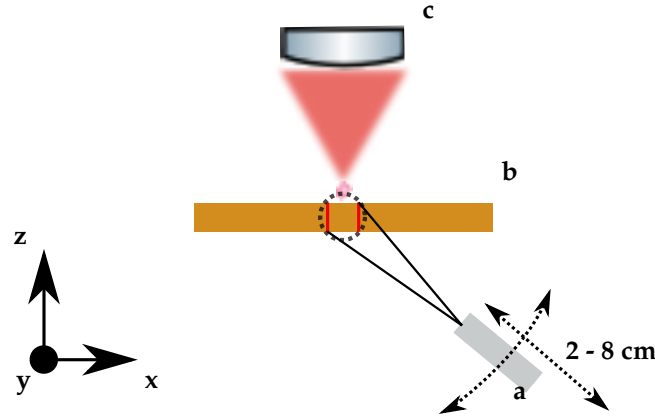


Figure 2.20: **Schematic (not to scale) to represent the application of magnetic field near the micro-diamonds on the CPW, using a permanent magnet.** A cylindrical shaped permanent magnet (a) is used near the CPW (b) and behind the confocal optics (c). The magnetic field magnitude and the direction is changed by changing the position of the permanent magnet as mentioned using dotted arrows. The conducting strip (two red lines) on the CPW represents the region where the micro-diamonds reside during the experiment. The dotted circle (Black) on the conducting strip, represents the spherical region in three dimension where the magnetic field strength need to be estimated.

The stray field near the micro-diamonds is required, to know the resultant vector magnetic field experienced at the zone. As shown in Fig. 2.22, the magnetic field strength components are measured at mentioned positions using the hall probe. They are measured and represented in [X,Y,Z] format with respect to a particular sign convention. The magnetic field components at A,B,C,D,E,F positions are tabulated in Table 2.1, with an uncertainty of 10 % due to the non calibrated hall probe. The sources of stray magnetic field are unknown and the resultant directions of the measured magnetic fields are found to be random. Hence, by averaging the field strengths at different spots, the resultant stray magnetic field strength is approximately estimated to be about ~1 Gauss with an unknown resultant direction.

²⁹Zeeman splitting and Rabi oscillations[Results]

³⁰An alloy of neodymium, iron, boron

³¹PCE-MFM 3000 Magnetic field measurement kit

³²The procedure is repeated for statistics

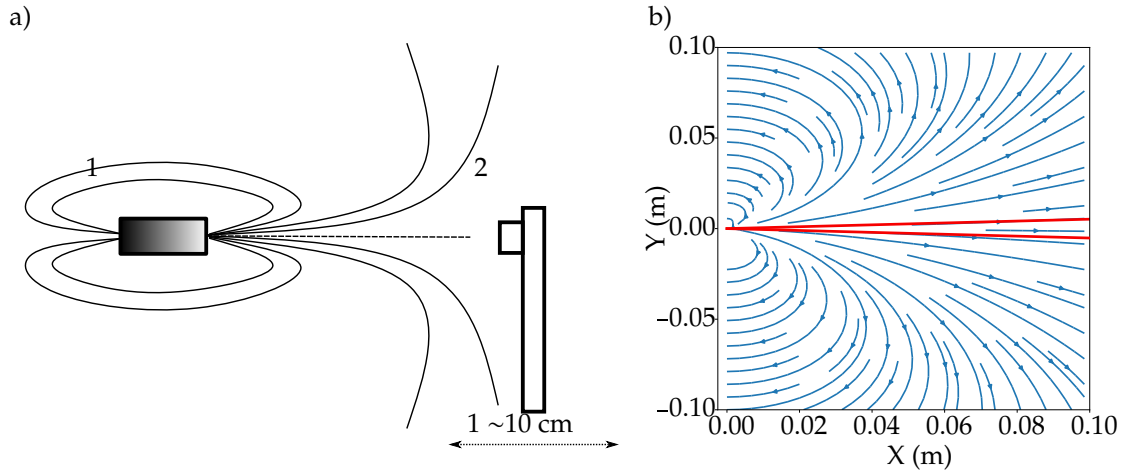


Figure 2.21: **Magnetic field strength measurement using a Hall probe (Not to scale) and the simulation of magnetic field in XY Plane.** a) Schematic of the magnetic field strength measurement procedure using hall probe(2) in the axial direction by varying the distance from 1 - 10 cm from the flat surface of the cylindrical permanent magnet(1) with an uncertainty of 0.1 cm. The data (blue) is plotted in Fig. 2.23. b) shows the simulation of two dimensional vector field plot due to the permanent magnet with a magnetization of 1~1.3 Tesla. The red lines represents a 6° uncertainty zone in the XYZ plane, leads to the uncertainty sphere schematically shown in Fig. 2.20. The inhomogeneous magnetic field contribution from this spherical region is simulated and taken into account as a confidence interval.

Points (Gauss)	A	B	C	D	E	F
X	0.6	-0.7	1	1	0.5	0.2
Y	0	-0.2	-0.1	1	-0.1	-0.3
Z	0.7	1	1	0	0.6	1

Table 2.1: **Stray field measurements at specific points mentioned in Fig.2.22.** All measurements are taken in six different directions using the hall probe with ~ 0.1 Gauss uncertainty. Average stray fields is mentioned with respect a specific sign convention.

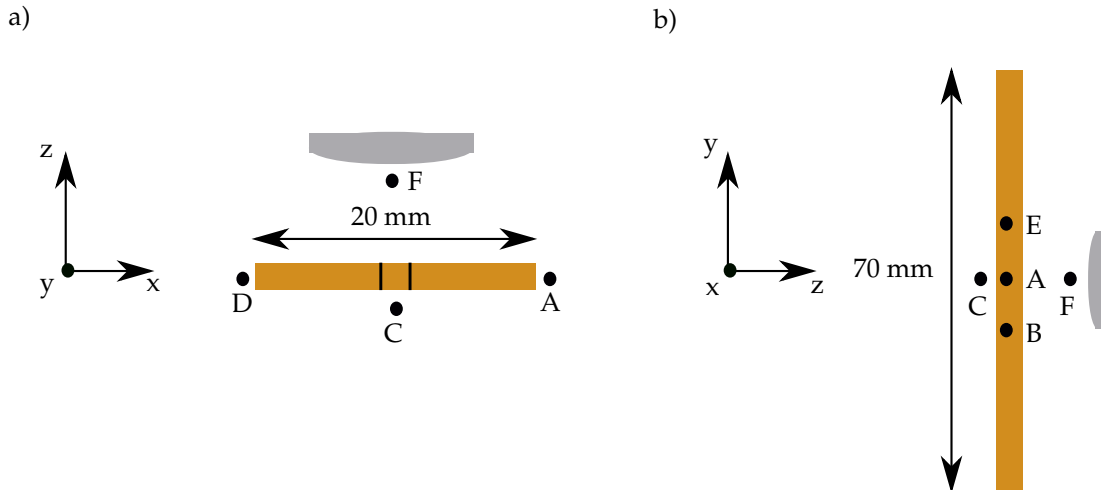


Figure 2.22: **Schematic overview of the stray field measurement near the coplanar waveguide (Not to scale).** a) represents the top-view of the apparatus, b) represents the lateral view. The magnetic field components along $[x,y,z]$ directions are measured using a hall probe and it is represented with respect to a sign convention. All averaged magnetic field components are tabulated in Table 2.1, with an uncertainty of ~ 0.1 Gauss. The resultant magnetic field vectors are randomly orientated near the CPW. By averaging the measured magnetic field strengths, the stray field magnitude near the conducting strip is assumed to be ~ 1 Gauss with an unknown resultant direction.

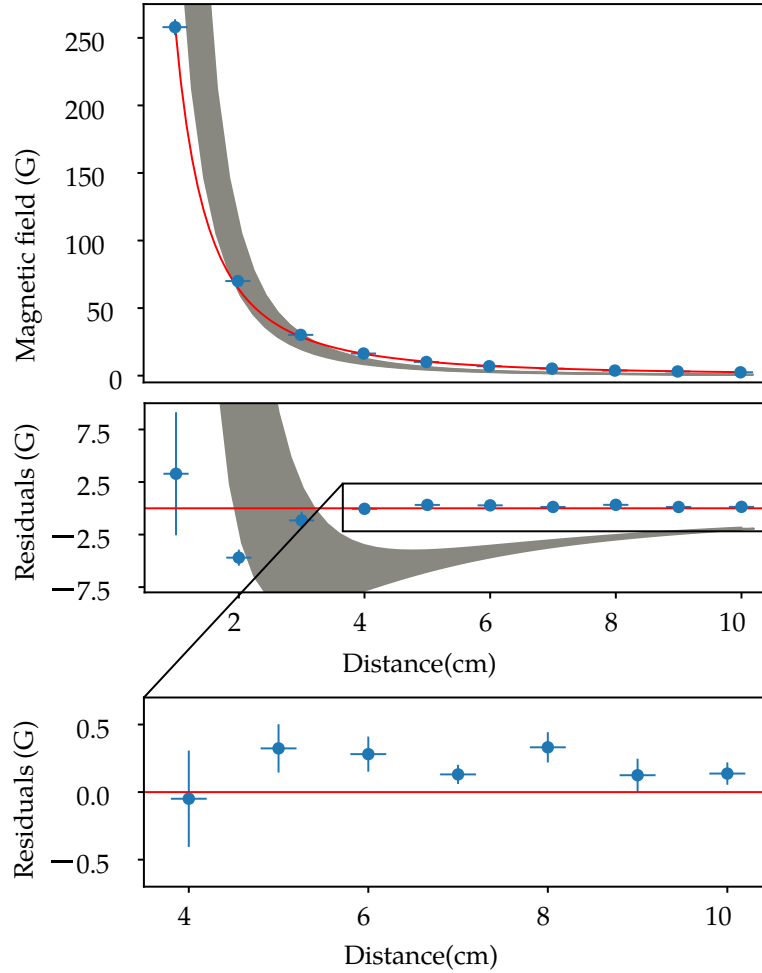


Figure 2.23: **Measurement and estimation of magnetic field strength due to a permanent magnet.** The data points (Blue) are measured by varying the hall probe from the surface of the magnets in axial direction. The red line represents a fit with $\frac{1}{x^2}$ model, we extract the coefficient of the model to be about $259(2) \text{ G/cm}^2$. The shaded region is a simulated zone, representing the magnetic field strength due to a cylindrical Nd permanent with a magnetization of $1\sim 1.3$ Tesla. The uncertainty due to the inhomogeneous field contribution in the spherical region represented in Fig. 2.20, is taken into account. From the data, a systematic shift in the measured data is observed. The residual plot represents the difference (Model fit - Measured Data points). The magnified portion of the residual plot is to show the errorbars corresponds to each measured data points.

Chapter 3

Results

In this chapter, we present results of the experiments performed with an ensemble of NV^- centers in the micro-diamonds. Firstly, the identification of NV^- centers and probing ground state spin manifolds are reported. Followed by its interaction with external perturbations such as magnetic and strain fields. Lastly, Rabi oscillation is performed over the addressed quantum spin manifolds and its coherence times are reported.

3.1 NV^- Identification

Monocrystalline micro-diamonds¹ with mean size of $\sim 25 \mu\text{m}$ in diameter and in random shapes, are used in the experiment. These diamonds are manufactured artificially using HPHT² method. During the annealing procedure of the method, the atmospheric impurities gets adsorbed into the lattice structure. As a result, the micro-diamonds are mentioned to occur in colors such as light gray to pale yellow[51]. Due to the lack of constraints over the shape and the concentration of impurities during the manufacturing process, the micro-diamonds occurs with asymmetric shapes and unaccounted amount of impurities which are inhomogeneously distributed in various regions of the diamond crystal.

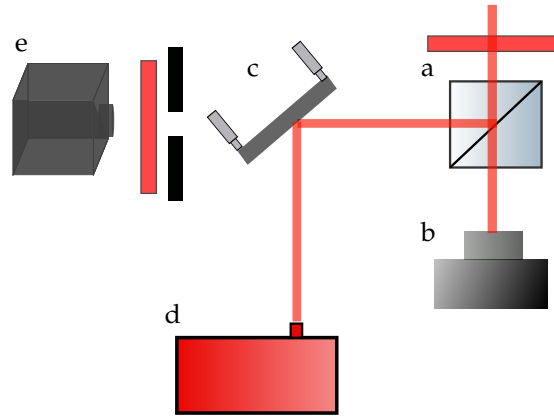


Figure 3.1: **Detection section of the experimental setup (Not to scale).** The optical beam containing fluorescence light from the diamond passes through the 90:10 beam splitter(a). 10 % of the overall light gets transmitted to reach the CMOS camera (b) and 90 % of the beam gets reflected. An adjustable mirror (c) is used to couple the light into the fiber coupling port of the grating spectrometer (d). The mirror (c) is removed during ODMR technique, to ensure the incidence of light on the PMT(e).

Using a wire tip, a few hundred micro-diamonds are taken and sprinkled over the conducting strip of the CPW. The CPW with its conducting surface facing the confocal optics, is attached to a position adjustable XYZ support. Using the micrometer screws of the XYZ support, the conducting strip of the CPW is aligned at the object plane of the confocal optics. The ability

¹Bought from MircoDiamant GMBH

²High Pressure High Temperature

to adjust the target under study, reduces the need to align all other optical components on the beam path to address different diamonds. The diode laser is made to operate in CW³ mode with less power⁴. The objective lens focuses the circularly polarized laser beam onto the CPW surface. The micrometer screws are adjusted coarsely to address a micro-diamond of choice on the CPW surface, with the focused laser beam. The laser light with its far-off resonance frequency eventually excites the NV centers present in the diamond crystal. The optical spectra emitted by the NV center during the radiative decay process, is collected by the objective lens. With the 4f imaging optics, the sub-micrometer features[Methods] are resolved and focused at the image plane. Due to the presence of the 90:10 beam splitter, 10 % of the overall fluorescence light reaches the CMOS camera. By fine tuning the micrometer screws of the XYZ support, a focused image of the micro-diamond is recorded using the CMOS camera. Using a composite Gaussian fit [Methods], the mean size of the diamonds is estimated and tabulated along with the respective exposure times in Table 3.1. The position of the micro-diamond with respect to the lab frame of reference is marked with the help of micrometers. The exposure settings of the CMOS camera is adjusted to record an unsaturated grayscale image of different diamonds named as Q,R,T as shown in Fig. 3.2. The selected exposure time gives an idea to compare the amount of color centers present in different diamonds. Since the laser excitation wavelength is far from the resonance of the NV⁻, other color centers present such as neutral NV centers may get excited and contributes to the overall fluorescence.

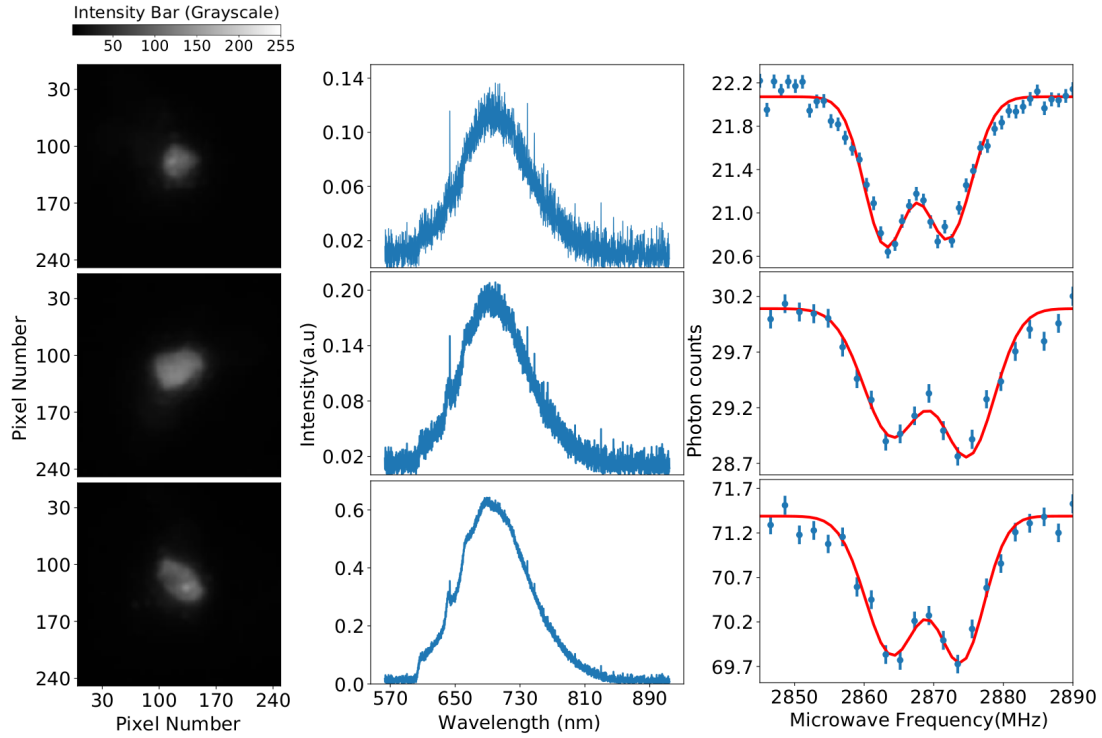


Figure 3.2: Diamonds with its image, optical spectra and ODMR spectra. Plots from left to right represents diamond images, optical spectra and its ODMR spectra. Firstly, the captured fluorescence images of the diamonds(Q,R,T) under focus using CMOS camera, are represented. Secondly, its corresponding optical spectra that spans from 600-800 nm is presented. All the optical spectra are acquired with same laser power. From the optical spectra, we observe a variation in intensity according to the amount of NV centers under focus. In addition, the ODMR spectra of the corresponding diamonds are presented. The contrast of the ODMR spectra[Table] is not observed to be linearly proportional to the amount of NV centers addressed.

The presence of negatively charged NV centre is confirmed, using the grating CCD spectrometer that can work in the range of 500 - 1000 nm. As shown in Fig. 3.1, an adjustable mirror is introduced into the detection section of the experimental setup in front of the PMT. The 90 % of the overall fluorescence light from the reflecting side of the beam splitter is redirected to reach

³Continuous output

⁴below 5mW

the fibre coupling port of the spectrometer. The systematic uncertainty due to a variation in the coupling angle of the light is reduced by optimising the fluorescence light using the adjustable mirror. By fine tuning the CPW position along with the help of spectrometer, various regions of a diamond are explored to address maximum NV^- centers. Hence, using the camera and the spectrometer, a region in the micro-diamond with maximum NV^- centers is resolved using the confocal optics. The optical spectra of an ensemble of NV^- centers present in the diamond, is recorded as shown in Fig. 3.2. For all the diamonds represented, the spectra spans across from 600-810 nm. A notch in the 600 nm of the spectra is due to the presence of longpass filter with a cutoff of 600 nm in front of the beam splitter in the optical path. From the spectra, the Zero-Phonon Line (ZPL) is observed at ~ 637 nm. This ZPL peak ensures the presence of NV^- centers present in the diamond crystal. The envelope that spans the whole optical spectra consists of various vibronic contributions from the lattice vibrations. The discrete phonon states cannot be deduced due to the unresolvable optical spectra. Using the ZPL contribution to the overall spectra of the diamond, the temperature of the diamond can be deduced with the help of Debye-Faller Factor[52]. The number of NV centers present in the various diamonds can't be estimated based on the acquired optical spectra, due to the inhomogeneous distribution of NV centers at various parts of the crystal. The collection efficiency of the optics and the isotropic emission of the NV^- limits the ability to quantify the number of NV^- centers.

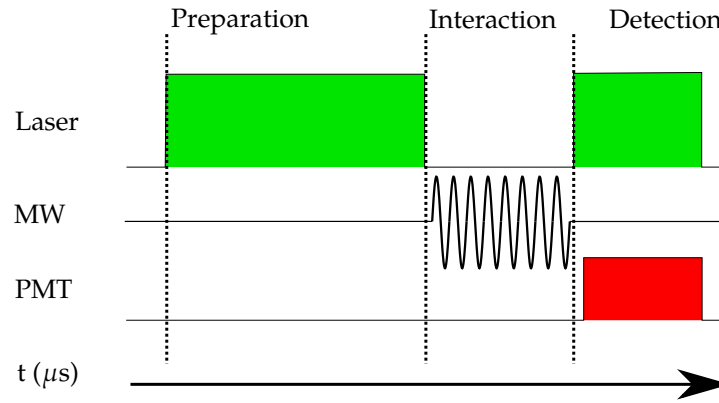


Figure 3.3: Schematic of the Pulsed Experimental sequence to acquire ODMR Spectra. This time critical pulse sequence is described in python code and executed via FPGA of the DAQ using ARTIQ. The sequence begins with preparation phase, where the laser is triggered to output for $\sim 150 \mu\text{s}$, using a TTL pulse from Digital I/O. Followed by interaction phase, the microwave signal of particular frequency is transmitted using CPW for ~ 200 ns, controlled via Urukul DDS, Frequency quadrupling circuit and Digital I/O. Finally the detection phase, the laser is triggered to output for $\sim 1 - 4 \mu\text{s}$ and the state detection is done with the PMT and output TTL pulses are recorded via input port of the Digital I/O.

The Zero-Field Splitting (ZFS) in the ground state spin of the NV^- center is detected using the Optically Detected Magnetic Resonance (ODMR) spectra. This technique ensures the presence of NV^- center in the diamond as well as helps in distinguishing the two non-degenerate manifolds of the spin system for sensing external perturbations. The operating mode of the diode laser is switched to pulse mode which outputs on trigger. The adjustable mirror is removed to allow the beam to enter the PMT. As shown in Fig. 3.3, the pulsed experimental sequence is deployed using the DAQ. The described experimental sequence is executed as a kernel from the FPGA, since it is time critical. At $t=0$, the rising edge of a TTL pulse from the digital I/O is made to trigger the laser output. The laser beam excites and initiates the fluorescence in the cluster of NV^- centers which are addressed with the confocal optics. The presence of the radiative decay and the non-radiative inter-system crossing mechanisms in the NV^- centers ensures the optical pumping of $m=0$ manifold of the ground state spin. The laser output is kept in output mode for $\sim 150 \mu\text{s}$ to pump the ground state manifold. This phase of the sequence is called as state preparation stage. Using the DAQ and frequency quadrupling setup, the microwave is tuned across the zero-field splitting frequency and transmitted near the diamonds with the help of CPW for a time period of ~ 200 ns. When the interacting microwave frequency resonates at the zero-field splitting frequency, a population transfer occurs from the $m=0$ manifold to the $m=\pm 1$ states. This phase of the sequence is called as interaction stage. Followed by the detection stage where the laser is ON for $\sim 1 \mu\text{s}$. The TTL events that are

produced by the PMT which corresponds to the photon number, is counted with the help of input port of the Digital I/O. The python code locally executed from the ARTIQ gets the data from the DAQ as it is interfaced with the FPGA via RPC⁵. The acquired data is archived in the form of datasets for analysis purposes. These acquired photon count corresponding to its respective interaction microwave frequency, for different diamonds are plotted in Fig. 3.2. From the plot, the reduction in the fluorescence level is observed at around 2870 MHz. This ODMR spectra represents the zero-field splitting resonance of the ground state spin of the addressed NV centers in the chosen diamond. The contrast of the two distinguished bright and dark states is affected by the magnitude of the interacting microwave field. Since the polarization vector is position dependent on the conducting surface of the CPW and the addressed diamonds are found randomly at different positions over the CPW. From the optical spectra and the ODMR spectra of the various diamonds represented in Table 3.1, the diamond named as T has more NV centers than all other diamonds. But the contrast in the ODMR spectra is observed to be low compared to others.

From the ODMR spectra, we observe two peaks separated by few megahertz across the ZFS frequency. This split between these two resonances, represents the E-parameter. By fitting a composite function with two Gaussian, the D- and E-parameter along with the contrast of the resonance and the fluorescence photon count with respect to a detection time of 3 μ s are tabulated for various diamonds in Table 3.1. As mentioned in the interaction Hamiltonian, the accessed spin manifold is prone to external perturbations and the consequences are observed in form of shifts in D- and E-parameters. The Zeeman effect $\frac{\mu_b}{\hbar} g S.B$ due to the stray magnetic field near the region of diamond under focus, is one of the contributing factor for the residual E-Parameter. From the stray field estimation, the magnetic field strength of ~ 1 Gauss contributes approximately 2.8 MHz between $m=-1$ and $m=+1$ states. Additionally, the presence of local stress in the crystal that deforms the C_{3v} symmetry and contributes to the E-parameter. On observation over various ODMR spectra of the different diamonds as given in Table 3.1, the local stress in the point defect varies for different diamonds due to various crystal properties as well as the stray magnetic field may vary as a result of different position of the diamonds in the lab frame of reference. These two factors provides an overall bottleneck in using the NV⁻ centers for quantifying any external perturbations with energies lower compared to these stray factors.

Diamond Name	Exposure (ms)	Cross section (μ m)	PL (counts)	Resonance Contrast	D (MHz)	E (MHz)
N	112	21.9(7), 18.6(3)	28.0(1)	0.056(4)	2870(1)	9(1)
O	328	19.2(3), 13.4(2)	15.8(1)	0.064(5)	2868(5)	8(5)
P	703	19.1(2), 19.0(4)	10.2(1)	0.048(7)	2869.4(4)	10.2(5)
Q*	185	13.8(3), 13.6(2)	22.07(6)	0.065(2)	2867.6(2)	9.0(2)
R*	159	22.4(4), 17.6(3)	30.1(1)	0.044(3)	2869.5(4)	11.0(4)
S	113	16.5(2), 28(1)	37.6(1)	0.047(3)	2869.1(5)	8.3(5)
T*	31	22.5(6), 21.2(4)	71.4(1)	0.023(2)	2869.0(4)	10.0(4)
U	153	15.5(3), 18.7(4)	35.1(1)	0.045(4)	2870(1)	7(1)

Table 3.1: **Observable features of the diamond from image and ODMR spectra.** For each diamond, the exposure settings of the CMOS camera, mean size of the diamond across XY coordinates, fluorescence in terms of photon count for a detection time of 3 μ s, contrast of the Zero-Field splitting along with D and E parameters, are presented.

⁵Remote Procedure call protocol

3.2 Influence of Laser power on Ground State Spin Dynamics

In this section, We report the influence of laser power on the NV^- with the help of observable changes in the ODMR spectra that represents ground state spin dynamics. Using the pulsed experimental sequence as shown in Fig. 3.3, the ODMR spectra of the chosen micro-diamond (T) is acquired using a low laser power⁶. From the ODMR spectra, we extract the D- and E-parameter to be 2869.0(4) MHz and 10.0(4) MHz respectively.

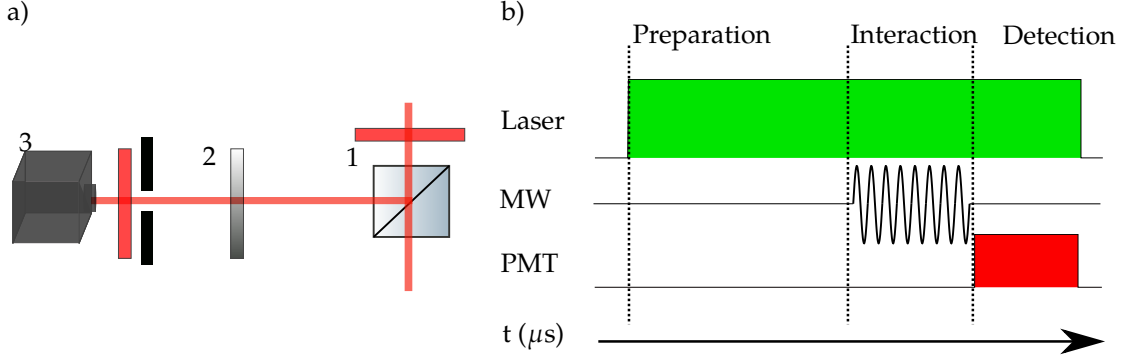


Figure 3.4: **Experimental set-up modification and the time critical experimental sequence.** a) In the detection section, on the reflecting side of the beam splitter(1), a ND filter(2) is introduced in front of the PMT(3). This modification is to stop the buffer memory of the FPGA from reaching saturation. b) The experimental sequence described is to understand the consequence of laser power interaction with the ground state spin of the NV^- -center. So, the laser is made to be in ON state during the interaction stage of the sequence. Apart from this change, rest of the sequence works alike pulsed experimental sequence.

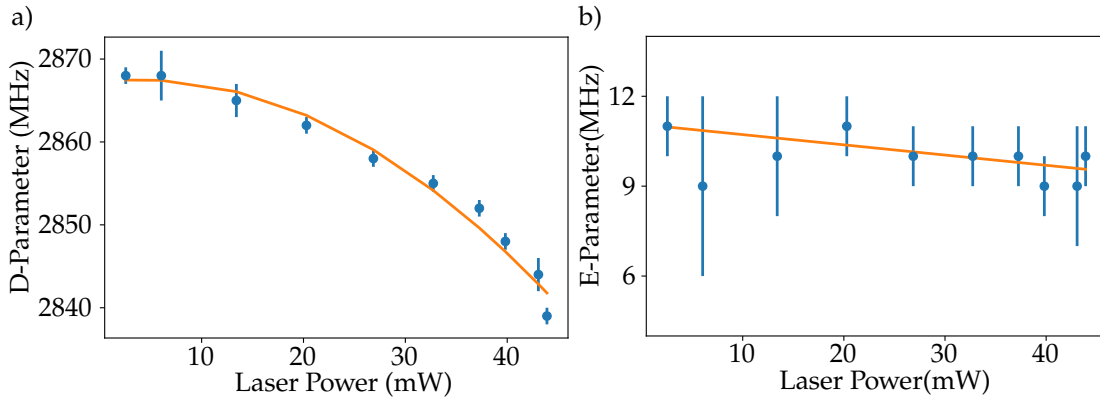


Figure 3.5: **D and E-Parameter extracted from the ODMR spectra.** a) represents the plot of D-parameter with respect to the change in laser power. The offset or the D-parameter at the lowest laser power represents the ZFS of the NV^- center at room temperature. Using a 2nd order polynomial fit over the non-linear response, we extract the coefficients 0.1(2) MHz/mW and -0.016(4) MHz/mW². b) represents the plot of E-parameter as a function of laser power. By fitting a linear model over the data, we notice that the slope is in agreement with zero, as a function of varying laser power.

To understand the influence of laser power on the ground state dynamics of the NV^- center, the sequence shown in Fig. 3.4 b) is used. A difference in the sequence compared to the ODMR sequence is that the laser is made to output, during the interaction stage. The experiment involves irradiation of the diamond with varying laser power. The fluorescence output of the diamond increases as a function of the laser intensity. The buffer memory of the FPGA that controls the time critical sequence can only register limited number of TTL events. Hence, increased number of the TTL events from the PMT due to increased fluorescence level, affects the experiment that is executed. A modification is made in the detection part of the experimental set-up as shown in Fig 3.4 a). A Neutral Density filter is introduced in front of the PMT

⁶ < 5 mW

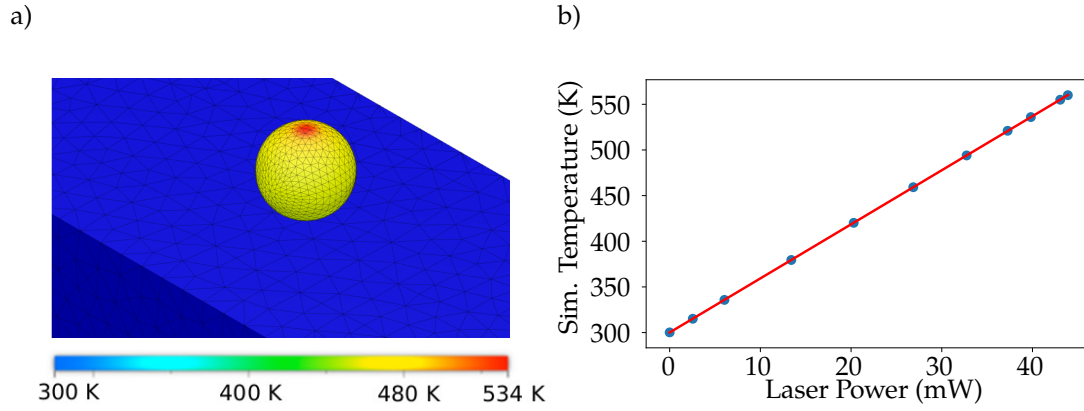


Figure 3.6: **Steady state thermal analysis using Finite Element Analysis in Autodesk Fusion 360.** a) shows the model created in the Autodesk software. The sphere represent a diamond with mean diameter of $25\ \mu\text{m}$ on top of the CPW. The region(red) on top represents the laser beam radiation incidence and the substrate(Blue) is at room temperature. The horizontal color bar represents the temperature distribution in different regions of the diamond. The simulation is done by giving 3 % of the total laser power on the laser beam region specified. By varying the laser power, the average temperature of the diamond extracted from the simulation is plotted as a function of laser power b). By fitting a linear model onto the simulated data, the change in temperature with respect to applied laser power is extracted as $\sim 6\ \text{K/mW}$.

that reduces the amount of photons. The detection time of the PMT is altered for various laser powers to compensate low photon rate as well as to maintain signal to noise ratio of the ODMR spectra.

The described experimental sequence is deployed from the DAQ using the ARTIQ system and is repeated for various laser powers. By fitting the composite function of two Gaussians model fit over the ODMR spectra acquired for various laser powers, the parameters that are coupled to external fields such as D- and E-parameters, are extracted. Figure 3.5 shows the plot, representing the D- and E-parameters variations with respect to the applied laser power. Comparing the non-linear response of the D-parameter with the respect to the applied laser power, to the literatures[52]. One of the reason for such a response of the D-parameter is found to be predominantly due to the heating of the micro-diamond. Though the experiments that are reported in various articles, are using passive heating to heat the diamond, the acquired data shows a similar response as reported earlier. By making a 2nd order polynomial fit over the D-parameter shift, we extract the coefficients to be $0.1(2)\ \text{MHz/mW}$ and $-0.016(4)\ \text{MHz/mW}^2$. The quadratic contribution to the response is from the electron-phonon interactions[19]. The temperature data from a literature[52] that uses passive heating technique on a diamond⁷, is compared. To get a shift in resonance of $\sim 30\ \text{MHz}$, a temperature of approximately 550 K is specified. From the data plot, the laser power of $\sim 40\ \text{mW}$ is expected to rise the temperature of the diamond to around 550 K. To estimate the amount of laser power that is absorbed from the laser beam, a Finite Element Analysis(FEA) is performed using the AUTODESK software as shown in Fig. 3.6 a). The micro-diamond along with the CPW is modeled and a region of laser beam is specified. By increasing the applied power on the specified region, the average temperature of the diamond simulated by the program is plotted as shown in Fig. 3.6 b). As an estimation, approximately 3 % of the total laser power is enough to rise the temperature of the diamond to such a level as mentioned. Using a linear model fit over the simulated data, we extract the change in temperature with respect to applied laser power to be about $\sim 6\ \text{K/mW}$. As the diamonds are not made with control over the impurity traces and its concentrations, the color centers along with the presence of para-magnetic nitrogen and hydrogen traces with absorption spectral lines in the visible range are some of the constituents responsible for the absorption of laser power. In the simulation, the temperature of the CPW is taken to be at room temperature. The high microwave power transmission through a strip with a considerable amount of transmission lose will eventually increase the temperature of the substrate. But it is taken to be insignificant since the microwave interaction stage lasts only

⁷with mean diameter of 30 nm

for 200 ns compared to the overall pulse duration of about 150 μ s. This overall simulation gives an approximate estimation of the temperature. Since the parameters such as specific heat capacity, bulk modulus, thermal expansion coefficient are taken to be fixed at a certain temperature window. It also certainly cannot take account of the NV⁻ centers present in the crystal structure and also treats the system as an amorphous substance.

One of the consequence, due to increase in temperature is a change in lattice structure. The locally experienced strain disrupts the molecular orbital, due to change in lattice constant of the unit cell and resulting in change in dipole moments in axial and non-axial directions of the C_{3v} symmetry. These changes in dipole moments translates and contributes to a local electric field change near the vacancy. It can be quantified with the help of observable changes in D- and E-parameter. From the observed responses, there is no significantly noticeable change in E-parameter. This peculiar response of the E-parameter can be used to justify the fact that the observed response in D-parameter is predominantly due to change in temperature of the system.

Equation 2 represents the spin-strain Hamiltonian[53] where the interaction of strain tensor in axial and non-axial directions are written based on the derived interactions from the electric field Hamiltonian.

$$H_{\epsilon} = H_{\epsilon 0} + H_{\epsilon 1} + H_{\epsilon 2}, \quad (2a)$$

$$H_{\epsilon 0}/h = [h_{41}(\epsilon_{xx} + \epsilon_{yy}) + h_{43}\epsilon_{zz}]S_z^2, \quad (2b)$$

$$H_{\epsilon 1}/h = \frac{1}{2}[h_{26}\epsilon_{zx} - \frac{1}{2}h_{25}(\epsilon_{xx} - \epsilon_{yy})]\{S_x, S_z\} + \frac{1}{2}(h_{26}\epsilon_{yz} + h_{25}\epsilon_{xy})\{S_y, S_z\}, \quad (2c)$$

$$H_{\epsilon 2}/h = \frac{1}{2}[h_{16}\epsilon_{zx} - \frac{1}{2}h_{15}(\epsilon_{xx} - \epsilon_{yy})](S_y^2 - S_x^2) + \frac{1}{2}(h_{16}\epsilon_{yz} + h_{15}\epsilon_{xy})\{S_x, S_y\} \quad (2d)$$

By assuming a homogeneous expansion in all three axis due to a change in temperature, the strain tensor can be approximated by taking off-diagonal elements to be zero[Appendix]. Hence, Equation 2 can be reduced to $H_{\epsilon} = H_{\epsilon 0}$ which represents electric field variation specific to the axial direction which corresponds to S_z component. Comparing it with the interaction Hamiltonian due to overall external perturbations, the final Hamiltonian to explain the ground state dynamics due to the influence of temperature can be written as shown in Eqn. 3. Hence, the D-parameter alone is found to be sensitive to homogeneous strain interactions such as change in temperature and E-parameter remains insensitive. The remaining terms of the Hamiltonian in Eqn 1, explains the residual stress due to symmetry breaking along with interactions due to stray fields.

$$H_{gs} = \frac{1}{\hbar^2}(D_{gs} + d_{||}E_z)S_z^2 \quad (3)$$

The spin-strain Hamiltonian is an approximate representation, considered for the C_{3v} symmetry. The DFT calculations mentioned in the article[53] and considerations doesn't reflect the whole consequences due to temperature change. The electron-phonon interactions are not understood through this formulation. A crystal with an ensemble of NV⁻ centers with broken C_{3v} symmetry demands complex model representation. But this interaction Hamiltonian is valid to understand certain properties of a microstate of an ensemble, during a temperature change.

3.3 Magnetic field sensing and Orientation of NV centers

In this section, we discuss the interaction of an externally applied DC magnetic field perturbations with the NV⁻ centers. As mentioned in the Hamiltonian, $\frac{\mu_b}{\hbar} g \vec{S} \cdot \vec{B}$ represents the interactions due to the magnetic field. The perturbations on the ground state triplet manifold of the NV center can be observed using the ODMR spectra that represents the zero-field splitting transition. The observable consequence due to the external magnetic field is in the form of change in E-parameter in the range of MHz as seen in stray magnetic field interaction. The E-parameter variation is linearly proportional to the applied magnetic field strength and this approximation holds until 0.1 T due to Anti-level crossing[45]. The projection of NV axes with the applied magnetic field, results in eight different transition in the ODMR spectra, corresponding to all four NV axis and its respective spin states. Using the Zeeman formalism, we can estimate the orientation of the NV centers in the crystal lattice using its interaction with externally applied DC magnetic field.

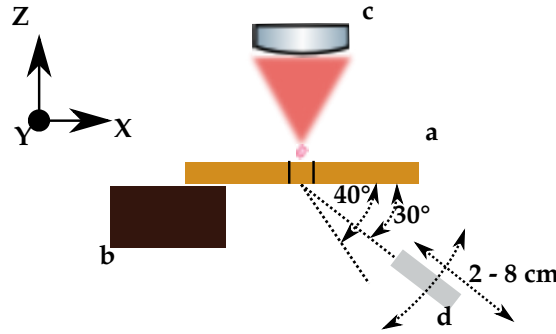


Figure 3.7: **Schematic (Not to scale) of the set-up with permanent magnet near the CPW for magnetic field sensing.** The coplanar waveguide (a) with Diamond Q on the conducting strip (marked with two lines), is attached with the XYZ support (b). A permanent magnet (d) is introduced at a specific angle and at specific distances to vary the resulting magnetic field strength and direction with respect to the confocal optics (c)

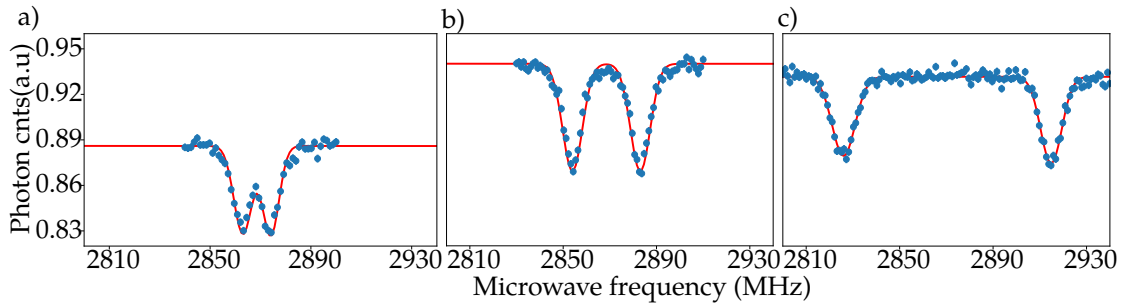


Figure 3.8: **ODMR spectra with respect to change in magnetic field strength due to magnet kept at 30° from X-axis.** a) ODMR spectra due to magnet kept at 7.5 cm from the CPW, E-parameter is measured to be ~10 MHz. b) Magnet at 4 cm from the CPW, E-parameter increases to ~30 MHz. c) Magnet at 2 cm from the CPW, E-parameter is measured to be ~90 MHz. Each peak have an unresolvable overlap of 4 Zeeman transitions that addresses all NV⁻ orientations. An unaccounted systematic shift in photon counts in the case of plot a), compared to other two spectra is observed. The width of the each transitions are accounted to estimate the uncertainty due to an unresolvable overlap of transitions.

Using the pulsed experimental sequence shown in Fig. 3.3, the ODMR spectra representing the zero-field splitting is acquired. Using the two Gaussian fit, we extract the observable parameters D and E parameters to be 2867.6(2) MHz and 9.0(2) MHz respectively. The residual E-parameter is the bottleneck and threshold for sensing DC magnetic fields that produces Zeeman transitions smaller than ~9 MHz. The D-Parameter is taken to be significantly constant throughout the experiment, since the described experimental sequence is performed at room temperature with constant laser power⁸.

⁸below 5 mW

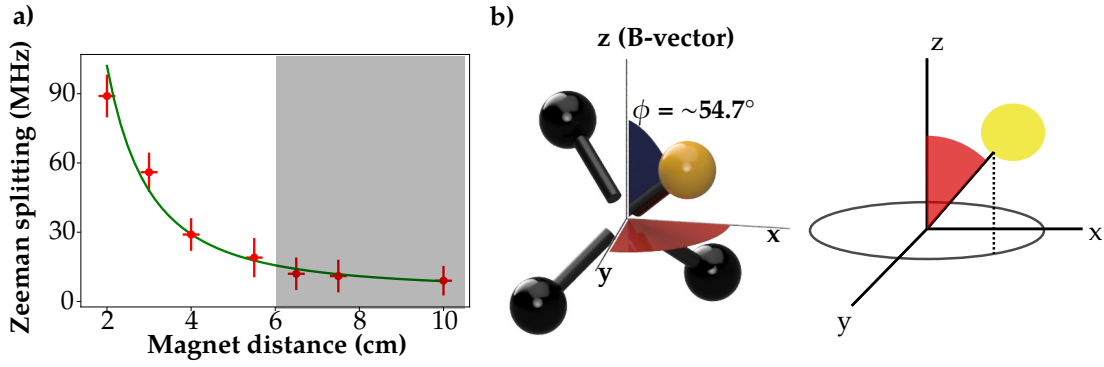


Figure 3.9: **Plot of Zeeman splittings due to the permanent magnet at 30° and the model of C_{3v} symmetry with respect to the field vector.** a) The plot (red) represents the E-parameters extracted from the ODMR spectra as function of distance of the magnet. Using a model fit that represents the dipole response, the coefficient of $\frac{1}{x^2}$ is extracted to be $388(33)$ MHz/cm² and the offset is $7(2)$ MHz. The data points in the shaded region is not considered for fitting. Because the effective magnetic field sensed, is in comparable order of magnitude with the estimated stray field. b) represents the model of crystal symmetry with respect to applied magnetic field vector which represents the z-axis. For readability, a simpler model representing [111] axis is drawn. The yellow circle represents the nitrogen and the angle of projection with z-axis is $\sim 54.7^\circ$ (Red). The black circle in the xy plane represents the unknown projection of [111] axis in the azimuthal plane.

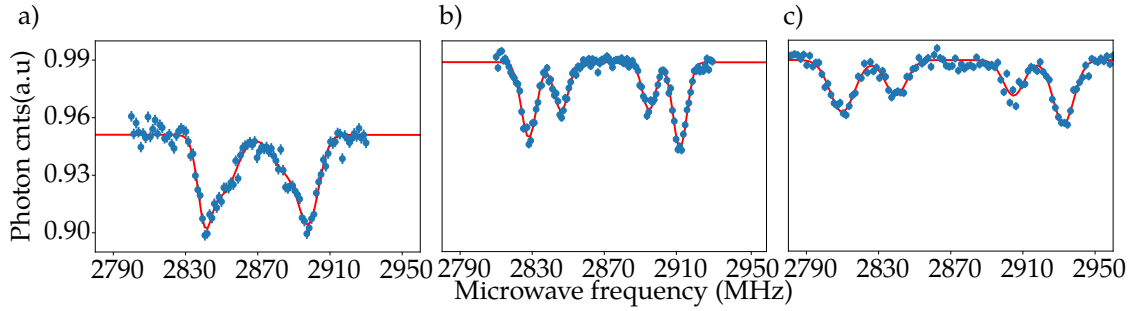


Figure 3.10: **ODMR spectra with respect to change in magnetic field strength due to magnet kept at 40° from X-axis.** a) ODMR spectra due to magnet at 3 cm away from the CPW. An overlap of multiple transitions are observed. By moving the magnet further to 2.5 cm, the plot b) shows four transitions with respect to two NV orientations. By moving the magnet further to 2 cm spot, c) shows an increase in E-parameter. The amplitude of transitions decrease as a result of increased magnetic field due to contributions from all other overlapping NV orientations. The corresponding Zeeman transitions are extracted, using a multiple Gaussian Model fit over the spectra.

The permanent magnet is introduced near the micro-diamond as shown in Fig. 3.7. By positioning the magnet at angle 30° with respect to the x-axis of the lab frame, the ODMR spectra is recorded using the pulse experimental sequence. The magnetic field strength is tuned by varying the position of the magnet (towards or away from the center position of the CPW) and the vector direction is approximately preserved. Using the pulsed experimental sequence, the ODMR spectra is recorded for the same diamond with different magnetic field and plotted as shown in Fig. 3.8. A Gaussian model fit with multiple Gaussian profiles, is made over the data to extract observables such as D- and E-parameters. The raw data shows a change in E-parameter symmetric around the D-parameter, as a function of changing magnet positions.

From the raw data, we observe two peaks separated by few MHz. There is an overlap of all Zeeman transitions due to 4 different NV⁻ axis. This spectra is possible when the magnetic field vector makes $\sim 54.7^\circ$ with respect to [111] direction of the lattice structure and all the probable NV⁻ axis experiences same effective magnetic field strength. Figure 3.9 a) shows the

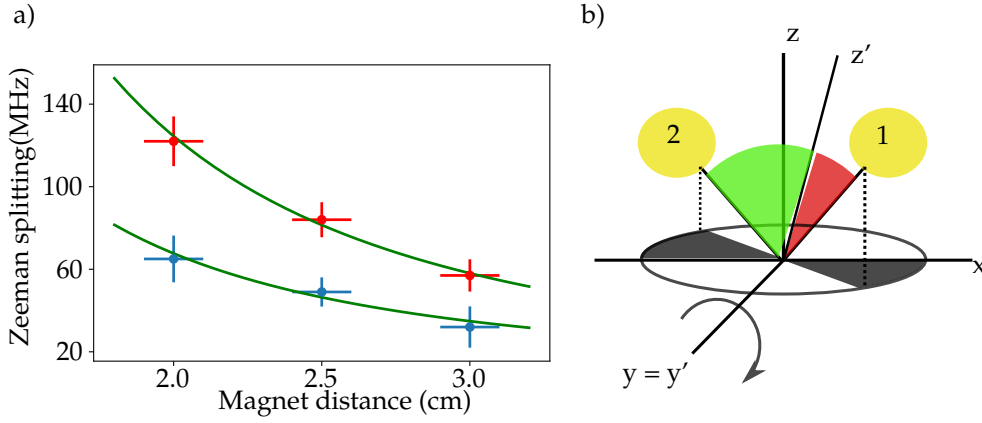


Figure 3.11: Plot of Zeeman Splittings due to permanent magnet at 40° and the vector model of C_{3v} symmetry. a) The plot (Red and Blue) represents the E-parameters extracted from the ODMR spectra with a multiple Gaussian model fit, as function of distance of the magnet. Using a model fit (Green) that represents the dipole response, the coefficients of $\frac{1}{x^2}$ are extracted for two different Zeeman transitions to be 478(42) and 236(58) MHz/cm² respectively. The offsets for two Zeeman transitions are 5(6) and 9(9) MHz respectively. b) shows the vector model of two different NV axis, where the magnetic field vector is changed by an angle of 10° in xz plane with respect to the previous case. Red and green zones represent the deduced projection angles 45(8)° and 70(8)° of the two NV axes, with respect to rotated magnetic field frame.

Zeeman splitting between $m=\pm 1$, with respect to different position of the magnet. Using the dipole response model fit over the data, we extract the coefficient of $\frac{1}{x^2}$ and the offset to be 389(33) MHz/cm² and 7(2) MHz respectively. The offset value is in agreement with the residual E-parameter, extracted from the ODMR under no external magnetic field condition. The data points in the shaded region is considered to be insignificant, since the effective magnetic field experienced by the NV centers are in comparable magnitude with the estimated stray field. From the estimated effective magnetic field coefficient and the NV axis angle as shown in Table 3.2, we calculate the magnetic field coefficient of the dipole response to be about 242(22) Gauss/cm² using Zeeman formalism $(\gamma B \cos(54.7^\circ))^9$. The unresolved projections of all NV orientations are accounted in the uncertainty of the calculated magnetic field strength. The calculated magnetic field coefficient using the NV⁻ center, is in agreement with the magnetic field calibration done using the Hall probe. Fig. 3.9 b) shows the C_{3v} symmetry with respect to the magnetic field vector which is represented as z-axis (xyz axis frame is with respect to magnetic field vector). With this set of measurements, the angle of [111] direction with respect to the azimuthal plane cannot be deduced. Hence, the NV axis([111] Plane) can have any orientation with respect to the azimuthal plane due to its symmetry.

Fit Parameter (MHz/cm ²)	Offset MHz	Effective coefficient B Field (Gauss/cm ²)	[111] angle w.r.t B field (θ)	Calculated coefficient B field (Gauss/cm ²)
389(33)	7(2)	139(12)	$\sim 54.7^\circ$	242(22)

Table 3.2: Estimation of the coefficient of magnetic field model with the help of Diamond Q. From the 30° case, the NV axis is estimated to make an angle $\sim 54.7^\circ$ with respect to magnetic field vector. From the effective magnetic field data, we calculate the coefficient of the dipole response using the diamond to be 242(22) Gauss/cm².

As shown in Fig. 3.7, the position of the magnet is changed to 40° spot with respect to the X-axis of the lab frame. In this position, the magnetic field strength is tuned by moving the magnet to three spots 3 cm, 2.5, 2 cm, by preserving the vector direction. The corresponding ODMR spectra are plotted as shown in Fig. 3.10. We observe four transitions in the spectra as a result of increase in magnetic field strength. From the raw data, we can expect each transition represents two different NV orientations. With respect to zero-field splitting symmetry, the Zeeman transitions are plotted as shown in Fig. 3.11 a). Using the dipole response model, we

⁹ $\gamma = 2.8 \text{ MHz/Gauss}$

extract the coefficients to be 478(42) MHz/cm² and 236(58) MHz/cm² corresponding to each transitions and their offsets to be 5(6) MHz and 9(9) MHz respectively. From the fit parameters, the corresponding effective magnetic fields are estimated. As shown in Fig. 3.11b), the change in magnet position in the xz plane by 10° is modeled as a rotation of frame of reference. In the rotated xz plane about y axis, z' represents the magnetic field vector. From the effective magnetic field coefficients, two NV axes are estimated to make 45(8)° and 70(8)° angles with respect to rotated frame of reference. From the simple vector models in Fig. 3.9 b) and 3.11 b), the projection ϕ angles of the NV⁻ axes with respect to xyz and x'y'z', are used to deduce the orientation of the diamond crystal with respect to the lab frame of reference XYZ[Appendix].

Magnet position w.r.t x-axis(θ)	Fit Parameter (MHz/cm ²)	Offset (MHz)	Effective B Field (Gauss/cm ²)	NV ⁻ Angles w.r.t B field (θ)
40°	478(42)	5(6)	171(15)	45(8)°
	236(58)	9(9)	84(21)	70(8)°

Table 3.3: Estimation of two NV axis projection with respect to rotated magnetic field vector reference.

In the lab frame of reference, as shown in Fig. 3.12, the NV⁻ axis [111] lies at an angle 5(8)° with respect to the Z axis(Lab frame). From the rotated magnetic vector measurements, the NV⁻ axis is estimated to reside at an angle 35(3)° to the XZ plane. The uncertainty is reduced considerably with the help of C_{3v} constraints. All other NV orientations can be deduced with the help of the quantized C_{3v} symmetry. The estimations can be improved by obtaining Zeeman splitting data for different magnetic field vectors. By obtaining eight transitions in the ODMR spectra with respect to all NV axis making different projections with the magnetic field vector, the orientation of the diamond crystal in the lab frame can be deduced with better precision.

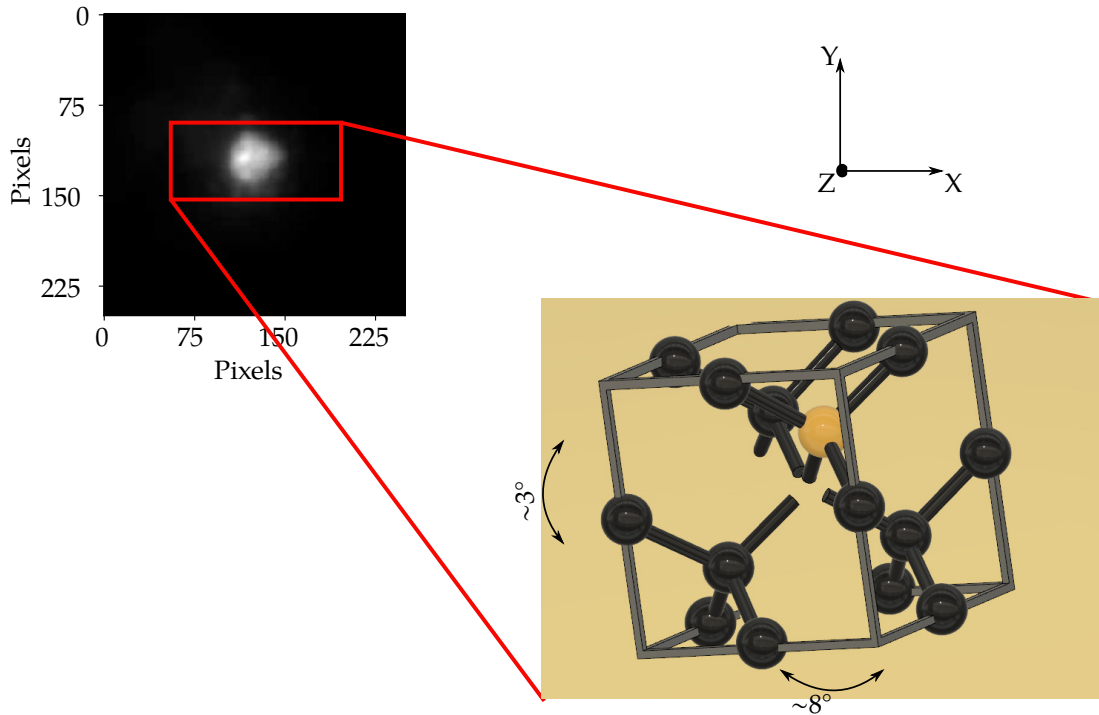


Figure 3.12: **Orientation of the mono-crystalline diamond(NV axis[111]) with respect to lab frame of reference.** From the estimations using two magnetic field vectors, the orientation of the NV axis is deduced[Appendix] and showcased. The NV axis(Yellow) surrounded by carbon(Black) is considered as [111] plane. The NV axis makes an angle 5(8)° with respect to the Z-axis. It makes an angle of 35(3)° with the XZ plane. The marked arrows shows the uncertainty of the diamond lattice with respect to lab frame. The uncertainty in the orientation is reduced with the help of C_{3v} symmetry and its orientation constraints.

3.4 Rabi Oscillations

In this section, the T_2 or the spin-spin relaxation time of the ground state spin manifolds is measured using the Rabi oscillations[54, 55]. An experimental sequence shown in Fig. 3.13, is used for performing Rabi oscillations. The interaction time $\sim t_{mw}$, is varied during the experiment by keeping the interacting microwave frequency constant. The microwave signal is tuned at resonance to enable coherent population transfer between two chosen sub-levels. By varying the microwave interaction time, the relaxation time of the coherent population dynamics is measured. As mentioned in literatures, some of the predominant reasons for the decoherence are interaction of the nuclear spins[56, 57], interaction of paramagnetic impurities[58] and the interactions of near surface NV^- centers with the fluctuating electric field noise[59].

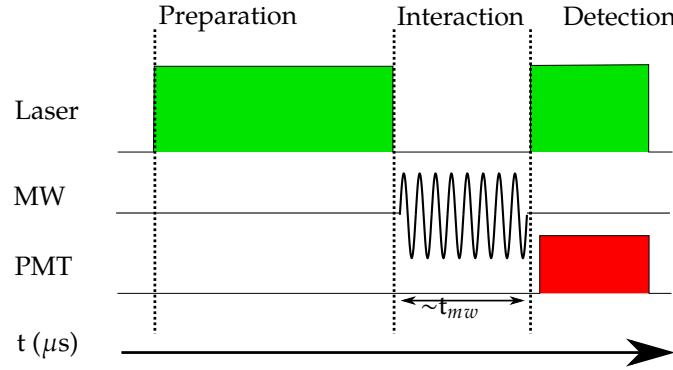


Figure 3.13: **Rabi Oscillation experimental sequence.** The interaction time of the microwave signal is varied over each repetitions(2000~4000) by fixing a constant microwave frequency to address a particular dipole transition. All other features and calibration constants are similar to the pulsed experimental sequence.

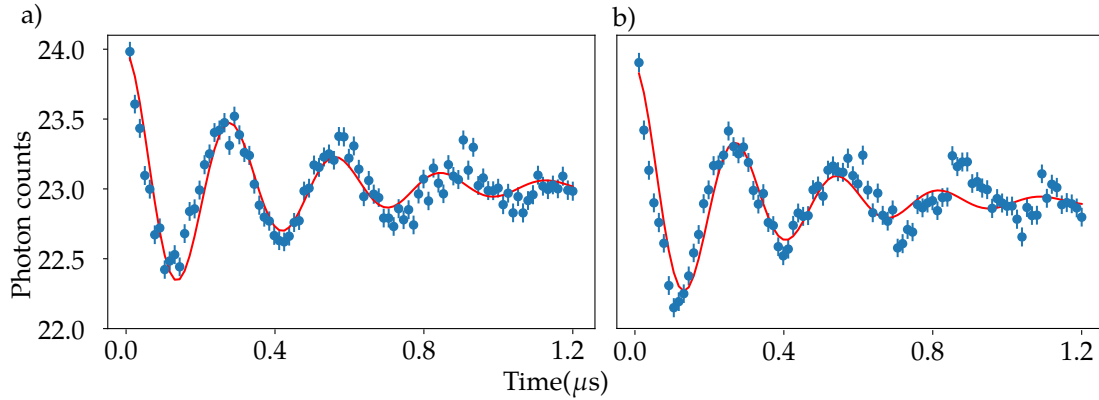


Figure 3.14: **Rabi Oscillations on two transitions at 2828 and 2913 MHz.** a) Plot of fluorescence with respect to microwave interaction time(Blue data points) represents the Rabi flops on the 2828 MHz resonance. Using a composite model fit, we extract the contrast of two levels, Rabi frequency and coherence time to be about 0.97(7), 3.53(3) MHz, 0.37(4) μs respectively. Similarly, b) represents the Rabi flops on the 2899 MHz. Using the same model fit, we estimate the amplitude, ω , τ to be 0.97(8), 3.66(4) MHz, 0.33(4) μs respectively.

From the Fig. 3.10 b), we observe the ODMR spectra to have four resonances. The two extreme transitions ~ 2828 MHz and ~ 2913 MHz, which represents two different NV^- axis, experiences an effective magnetic field of ~ 30 Gauss. The Rabi experimental sequence is performed on those two resonances as shown in Fig. 3.14. A composite model of $A \cos(\Omega t) \cdot \exp(-t/\tau)$ is fitted onto the raw data which describes an oscillatory and a relaxation response. We extract the observable parameters such as amplitude A of the Rabi flops that describes the contrast of the chosen two levels, Rabi frequency Ω_{12} and the coherence time τ as shown in Table 3.4. The Rabi frequency is proportional to the projection of magnetic field component of the microwave field with the addressed dipole moment. According to the characteristics of the CPW¹⁰, the

¹⁰Coplanar waveguide

transmitted microwave field is polarized and propagates as a TEM wave. The chosen dipole moment belongs to an ensemble of NV^- centers, orientated in two different directions. Due to the quantization axis of the applied magnetic field vector, the sub-levels show degenerate energies in the ODMR spectra. As a result, two different NV axis are expected to make different projections with the interacting magnetic field component of the microwave field. Hence, the observed Rabi flops has contributions from two different Rabi frequencies along with detuned contributions δ from an ensemble of unresolved transitions near the driven transition as shown in Eqn. 4.1. Therefore, this model is not suitable to understand the decoherence due to nuclear spins, impurities etc. The extracted coherence time represents decoherence due to population dynamics of an ensemble with different Rabi frequencies. This overshadows other factors that promotes decoherence in the addressed two-level system.

$$\sum \Omega \propto d_{12}^1 \cdot \vec{B}_1 + d_{12}^2 \cdot \vec{B}_2 + \delta \quad (4.1)$$

Effective magnetic field(Gauss)	Resonances (MHz)	Amplitude (Photons)	Rabi Frequency(MHz)	Coherence time (μs)
~30	2828	0.97(7)	3.53(3)	0.37(4)
	2913	0.97(8)	3.66(4)	0.33(4)

Table 3.4: **Observable parameters from the Rabi oscillations.** The extracted parameters using the Rabi composite fit is presented for two different transitions on the same diamond (Diamond Q).

The coherence time of the Rabi flops, can be improved by choosing a two-level that only represents one specific NV^- axis. The possibility can be ensured with the magnetic field vector that makes non-degenerate projection with all 4 NV^- orientations. This reduces decoherence due to contributions from microwave field interactions with all other NV orientations. By application of magnetic field vector parallel to the NV axis, the influence of nuclear spins, paramagnetic impurities and spectator NV centers on the spin-spin relaxation times are reported to decrease[56]. By executing complex quantum control sequences[7, 60], the environmental interactions can be actively decoupled from affecting the T_2 time of the chosen two-level Quantum system.

Chapter 4

Discussion and Outlook

In this work, we have assembled a benchmark experimental consisting of a confocal optics, data acquisition system and a coplanar waveguide(CPW), to address an ensemble of NV^- centers present within the artificially synthesized micro-diamonds. Subsequently, using the confocal imaging optics a spatial resolution of $\sim 0.3 \mu\text{m}$ is achieved. A frequency quadrupling circuit is developed and interfaced to work with the data acquisition system to generate microwave signals in a range of 2600~3000 MHz. The overall experimental set-up is programmed and calibrated to execute time-critical experimental sequences with a temporal resolution of 1 ns and to perform quantum methodologies. Using these control fields, specific internal electronic states(ground state spin manifolds) of the NV^- centers are accessed. The inherent quantum properties of the addressed states, its interactions and the corresponding consequences due to stray local strain, electric and magnetic fields are documented. Using magnetic field sensing property of the NV^- , the orientation of the diamond crystal structure with respect to the lab frame of reference is deduced within $\sim 10\%$ uncertainty. The response of the addressed electronic states of the NV^- centers to the change in laser power is observed and its underlying physics is partially understood with the help of spin-strain Hamiltonian of the C_{3v} symmetry. By optimizing the control fields, the Rabi oscillations are performed on the addressed states in an ensemble of NV^- centers and its coherence time of $\sim 0.30 \mu\text{s}$ is estimated. Through our experiments, we showcase the ability of the NV^- centers for sensing and for information processing. Subsequently, the ability of our experimental set-up to perform time-critical quantum experiments such as Rabi flops is ensured.

Using diamonds with single defects or engineered CVD diamonds with specified NV axis will enhance the sensing abilities[61]. By controlling the environmental conditions near the CPW, we can get better insights into the interactions of the probed electronic states of the NV^- centers with the external fields. Implementing a tunable, comparably homogenous magnetic field source like Helmholtz coil, largely reduces the uncertainty due to repositioning of the permanent magnets. Optimising these control fields can improve the sensitivity of the addressed electronic states of the NV^- centers. High sensitivity quantum sensing can be implemented using various quantum protocols such as Ramsey[62], Spin-echo[60] and other sequences like Carr-Purcell-Meiboom-Gill[7]. A compact trap device has to be designed[63] with control electrodes along with capabilities to transmit control fields(Microwave), to implement control over the external and internal degrees of freedom of the levitated micro-diamonds. Altogether, the improvements that are envisioned may lead to a robust trapped quantum sensor that can be used in ambient conditions for physics, chemistry, nanotechnology and biological applications.

Appendix A

Spin-strain interactions

TEMPERATURE EFFECT

Interaction Hamiltonian of the ground state spin of NV^-

$$\hat{H}_{gs} = \frac{1}{\hbar^2} (D_{gs} + d_{11} E_z) S_z^2 + \frac{\mu_B}{\hbar} g \vec{S} \cdot \vec{B} - \frac{1}{\hbar^2} d_{\perp} E_x (S_x^2 + S_y^2) + \frac{1}{\hbar^2} d_{\perp} E_y (S_x S_y + S_y S_x)$$

where E_x, E_y, E_z represents electric field due to External applied fields along with strain, stress interactions.

The spin-strain interaction Hamiltonian that addresses C_{3v} symmetry is written as

$$H_E = H_{E0} + H_{E1} + H_{E2},$$

$$H_{E0}/\hbar = [h_{41}(\epsilon_{xx} + \epsilon_{yy}) + h_{43} \epsilon_{zz}] S_z^2,$$

$$H_{E1}/\hbar = \frac{1}{2} [h_{26} \epsilon_{zx} + \frac{1}{2} h_{25} (\epsilon_{xx} - \epsilon_{yy})] \{S_x, S_z\} + \frac{1}{2} (h_{26} \epsilon_{yz} + h_{25} \epsilon_{xy}) \{S_y, S_z\}$$

$$H_{E2}/\hbar = \frac{1}{2} [h_{16} \epsilon_{zx} - \frac{1}{2} h_{15} (\epsilon_{xx} - \epsilon_{yy})] (S_y^2 - S_x^2) + \frac{1}{2} (h_{16} \epsilon_{yz} + h_{15} \epsilon_{xy}) \{S_x, S_y\}$$

Due to increase in temperature, the strain tensor will become,

$$\begin{pmatrix} 1 & 0 & 0 \\ 0 & 1 & 0 \\ 0 & 0 & 1 \end{pmatrix}, \text{ where all off-diagonal elements are zero.}$$

Hence, $\epsilon_{xx}, \epsilon_{yy}, \epsilon_{zz} = 1$ and $\epsilon_{ij} = 0$

The spin-strain hamiltonian can be written as

$$H_E = H_{E0} + H_{E1} + H_{E2}$$

From DFT calculations in literature, the coefficients are calculated, But it is not needed to describe the response.

$$H_E = H_{E0} = [h_{41} (\epsilon_{xx} + \epsilon_{yy}) + h_{43} \epsilon_{zz}] S_z^2$$

the resultant hamiltonian of ground state that describes the influence of temperature is

$$\hat{H}_{gs} = \underbrace{\frac{1}{\hbar^2} (D_{gs} + d_{11} E_z) S_z^2}_{\text{affected by Temperature change}} + \underbrace{\frac{\mu_B}{\hbar} g \vec{S} \cdot \vec{B} - \frac{1}{\hbar^2} d_{\perp} E_x (S_x^2 + S_y^2) + \frac{1}{\hbar^2} d_{\perp} E_y (S_x S_y + S_y S_x)}_{\text{Strain magnetic \& Strain C3v Symmetry}}$$

Appendix B

Estimation of NV orientations with the help of Zeeman effect

- From the $\sim 30^\circ$ case: The NV axis is estimated to make $\sim 54.7^\circ$ with the magnetic field vector.
- From the $\sim 40^\circ$ case: Two zeeman transitions observed, the corresponding projections are deduced.
- C_{3v} symmetry is modelled, along with two magnetic field vectors. Constrains are made based on the deduced projections to find the orientation of the NV axis with the uncertainty bounds.
- From the model, we estimate the projection of NV axis in the XZ plane to be $35(3)$. Other projections outside the uncertainty bound will lead to additional zeeman transitions in the spectra.

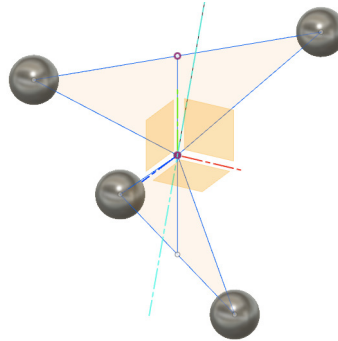


Figure B.1: Modelled C_{3v} symmetry with two magnetic field vectors, all the spheres corresponds to probable positions of Nitrogen atom in the lattice structure.

Appendix C

Python codes [Kernel and Host code]

Laser Modulation Calibration Code

```
# -*- coding: utf-8 -*-
"""
Created on Thu Jul 12 22:23:09 2018

@author: Ulrich Warring & Deviprasath Palani
"""
import numpy as np
from artiq.experiment import *
#file needed for all standard artiq conversions
import std_include

class laser_sw_test(EnvExperiment):

    def build(self):
        self.setattr_device("core")
        self.setattr_argument("t_delay", Scannable(default=RangeScan(0.01, 0.1, 10),ndecimals=3))
        self.setattr_argument("t_det", NumberValue(default=1.2,ndecimals=2))
        self.setattr_argument("N_pts", Scannable(default=RangeScan(1, 1000, 1000),ndecimals=0))
        self.setattr_argument("N_exp", NumberValue(default=150,ndecimals=0, step=1))
        self.setattr_device("urukul0_ch0")

        for ch in range(8):
            self.setattr_device("ttl{}".format(ch))

    @rpc(flags={"async"})
    def monitor(self, x, y):
        print("Pt: {}".format(x), " / {}".format(y))

    @kernel
    def std_init(self):
        self.core.break_realtime()
        delay(.5*ms)
        self.core.reset()

    @kernel
    def exp(self, t_delay, t_det, N_exp):
        self.set_dataset("counts", np.full(self.N_exp,0.000),broadcast=True)
        for k in range(N_exp):
            self.core.break_realtime()
            self.ttl2.gate_rising(t_det*us)
            #N_bg = self.ttl2.count()
            self.core.break_realtime()

            self.ttl6.on()
            self.ttl2.gate_rising(t_det*us)
            #N_norm = self.ttl2.count()
            self.ttl6.off()
            self.core.break_realtime()

            self.ttl6.on()
            self.ttl7.on()#monitoring ttl
            self.core.break_realtime()

            delay(10 * us)

            self.ttl6.off()
            self.ttl7.off()#monitoring ttl
            delay(t_delay * us)
            self.ttl2.gate_rising(t_det*us)
```



```

        N_photons = (self.ttl2.count()) #/ (N_norm - N_bg)
        delay(10*us)

        self.mutate_dataset("counts",k, N_photons)

def run(self):
    l = len(self.t_delay)
    self.set_dataset("data_x",np.full(l,np.nan),broadcast=True)
    self.set_dataset("data_y",np.full(l,np.nan),broadcast=True)
    self.set_dataset("data_yerr",np.full(l,np.nan),broadcast=True)
    for i,f in enumerate(self.t_delay):
        self.std_init()
        #freq = std_include.freqX4(f)
        self.exp(f, self.t_det, self.N_exp)
        #Analyzing phase
        counts = self.get_dataset("counts")
        mean_counts = np.mean(counts)
        std_counts = np.std(counts) / np.sqrt(self.N_exp)
        self.monitor(f, mean_counts)
        self.mutate_dataset("data_x",i,f)
        self.mutate_dataset("data_y",i,mean_counts)
        self.mutate_dataset("data_yerr",i,std_counts)

```

Pulsed Experimental Sequence[ODMR, Zeeman, Rabi]

- For ODMR and Zeeman: Experiment sweeps across the frequency range with fixed Microwave interaction time.
- For Rabi: Experiment iterates over the interaction time for fixed microwave frequency.

```

# -*- coding: utf-8 -*-
"""
Created on Thu Jul 12 22:23:09 2018

@author: UW & DP
"""
import numpy as np
from artiq.experiment import *
#file needed for all standard artiq conversions
import std_incl

class mw_fscan(EnvExperiment):

    @rpc(flags={"async"})
    def monitor(self, x, y, z):
        print("Pt.#{0}".format(x), " at: {0}".format(y), " / {0}".format(z))

    @kernel
    def std_init(self):
        self.core.reset()
        self.urukul0_ch0.init()

    @kernel
    def std_prep(self, t_prep, t_delay_laser):
        self.ttl6.on()
        delay((t_prep-t_delay_laser) * us)
        self.ttl6.off()
        delay(t_delay_laser * us)

    @kernel
    def std_det(self, t_det, t_delay_laser):
        self.ttl6.on()
        delay(t_delay_laser*us)
        self.ttl2.gate_rising(t_det*us)
        self.ttl6.off()
        delay(t_delay_laser*us)
        return self.ttl2.count()

    @kernel
    def mw_pulse(self, fr_mw, t_mw, att_mw, mw_phase):
        self.urukul0_ch0.set_att(att_mw*dB)
        delay(1*ns)
        self.urukul0_ch0.set(fr_mw*MHz, phase=mw_phase/4)
        delay(1*ns)

        with parallel:
            self.urukul0_ch0.sw.on()
            self.ttl7.on()

        delay(t_mw * us)

        with parallel:
            self.urukul0_ch0.sw.off()
            self.ttl7.off()

    @kernel

```

```

def exp(self, t_prep, fr_mw, t_mw, att_mw, t_det, t_delay_laser, N_exp):
    for k in range(N_exp):
        self.core.break_realtime()
        self.std_prep(t_prep, t_delay_laser)

        #mw pulses
        self.mw_pulse(fr_mw, t_mw, att_mw, 0.0)

        N_photons = self.std_det(t_det, t_delay_laser)
        self.mutate_dataset("counts", k, N_photons)

def build(self):
    self.setattr_device("scheduler")
    self.setattr_argument("graceful_termination", BooleanValue(True))
    self.setattr_device("core")
    self.setattr_device("urukul0_ch0")
    for ch in range(8):
        self.setattr_device("ttl{}".format(ch))

    self.setattr_argument("fr_mw", Scannable(default=RangeScan(2800, 2940, 50),
        ndecimals=8))

def prepare(self):
    l = len(self.fr_mw)
    self.set_dataset("data_x",
        np.full(l, np.nan),
        broadcast=True)
    self.set_dataset("data_y",
        np.full(l, np.nan),
        broadcast=True)
    self.set_dataset("data_yerr",
        np.full(l, np.nan),
        broadcast=True)
    self.set_dataset("counts",
        np.full(np.int(self.get_dataset("std.N_exp", archive=False)), np.nan),
        broadcast=True)

    self.set_dataset("t_prep", self.get_dataset("std.t_prep", archive=False), broadcast=False, persist=False, save=True)
    self.set_dataset("fr_mw", self.get_dataset("std.fr_mw", archive=False), broadcast=False, persist=False, save=True)
    self.set_dataset("t_mw", self.get_dataset("std.t_mw", archive=False), broadcast=False, persist=False, save=True)
    self.set_dataset("att_mw", self.get_dataset("std.att_mw", archive=False), broadcast=False, persist=False, save=True)
    self.set_dataset("t_det", self.get_dataset("std.t_det", archive=False), broadcast=False, persist=False, save=True)
    self.set_dataset("N_exp", self.get_dataset("std.N_exp", archive=False), broadcast=False, persist=False, save=True)

def run(self):
    i=0
    for scan_var in self.fr_mw:

        self.std_init()

        #exp(self, t_prep, fr_mw, t_mw, att_mw, t_det, t_delay_laser, N_exp)
        self.exp(
            self.get_dataset("std.t_prep", archive=False),
            std_incl.freqX4(scan_var),
            self.get_dataset("std.t_mw", archive=False),
            self.get_dataset("std.att_mw", archive=False),
            self.get_dataset("std.t_det", archive=False),
            self.get_dataset("cal.delay_laser", archive=False),
            np.int(self.get_dataset("std.N_exp", archive=False))
        )

        #store data
        counts = self.get_dataset("counts")
        mean_counts = np.mean(counts)
        std_counts = np.std(counts) / np.sqrt(np.int(self.get_dataset("std.N_exp", archive=False)))

        self.monitor(i, scan_var, mean_counts)

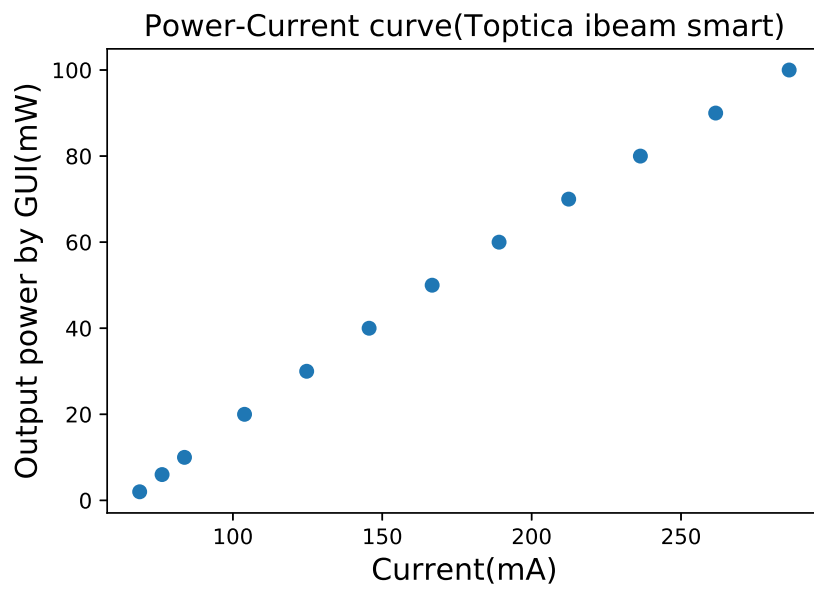
        self.mutate_dataset("data_x", i, scan_var)
        self.mutate_dataset("data_y", i, mean_counts)
        self.mutate_dataset("data_yerr", i, std_counts)

        i += 1

```

Appendix D

Power-Current calibration curve



Bibliography

- [1] F Jelezko, C Tietz, A Gruber I Popa, A Nizovtsev, S Kilin, and J Wrachtrup. Spectroscopy of Single N-V Centers in Diamond. 2:255–260, 2001.
- [2] Marcus W. Doherty, Neil B. Manson, Paul Delaney, Fedor Jelezko, Jörg Wrachtrup, and Lloyd C.L. Hollenberg. The nitrogen-vacancy colour centre in diamond. *Physics Reports*, 528(1):1–45, jul 2013.
- [3] Romana Schirhagl, Kevin Chang, Michael Loretz, and Christian L. Degen. Nitrogen-Vacancy Centers in Diamond: Nanoscale Sensors for Physics and Biology. *Annual Review of Physical Chemistry*, 65(1):83–105, apr 2014.
- [4] Yiwen Chu. *Quantum optics with atom-like systems in diamond*. PhD thesis, Harvard, 2014.
- [5] C. L. Degen, F. Reinhard, and P. Cappellaro. Quantum sensing. *Reviews of Modern Physics*, 89(3):035002, jul 2017.
- [6] J. R. Maze, P. L. Stanwix, J. S. Hodges, S. Hong, J. M. Taylor, P. Cappellaro, L. Jiang, M. V. Gurudev Dutt, E. Togan, A. S. Zibrov, A. Yacoby, R. L. Walsworth, and M. D. Lukin. Nanoscale magnetic sensing with an individual electronic spin in diamond. *Nature*, 455(7213):644–647, oct 2008.
- [7] J. M. Taylor, P. Cappellaro, L. Childress, L. Jiang, D. Budker, P. R. Hemmer, A. Yacoby, R. Walsworth, and M. D. Lukin. High-sensitivity diamond magnetometer with nanoscale resolution. *Nature Physics*, 4(10):810–816, oct 2008.
- [8] F. Dolde, H. Fedder, M. W. Doherty, T. Nöbauer, F. Rempp, G. Balasubramanian, T. Wolf, F. Reinhard, L. C. L. Hollenberg, F. Jelezko, and J. Wrachtrup. Electric-field sensing using single diamond spins. *Nature Physics*, 7(6):459–463, jun 2011.
- [9] P. Maletinsky, S. Hong, M. S. Grinolds, B. Hausmann, M. D. Lukin, R. L. Walsworth, M. Loncar, and A. Yacoby. A robust scanning diamond sensor for nanoscale imaging with single nitrogen-vacancy centres. *Nature Nanotechnology*, 7(5):320–324, may 2012.
- [10] Linh M. Pham. Magnetic field sensing with nitrogen-vacancy color centers in diamond. Technical report, DTIC Document, 2013.
- [11] Thomas Wolf, Philipp Neumann, Kazuo Nakamura, Hitoshi Sumiya, Takeshi Ohshima, Junichi Isoya, and Jörg Wrachtrup. Subpicotesla Diamond Magnetometry. *Physical Review X*, 5(4), oct 2015.
- [12] Simon Schmitt, Tuvia Gefen, Felix M Stürner, Thomas Uden, Gerhard Wolff, Christoph Müller, Jochen Scheuer, Boris Naydenov, Matthew Markham, Sebastien Pezzagna, Jan Meijer, Ilai Schwarz, Martin Plenio, Alex Retzker, Liam P McGuinness, and Fedor Jelezko. Submillihertz magnetic spectroscopy performed with a nanoscale quantum sensor. *Science*, 837(May):832–837, 2017.
- [13] A Brunner, J H Shim, D Suter, H Sumiya, J Isoya, and J Wrachtrup. High-Precision Nanoscale Temperature Sensing Using Single Defects in Diamond. *Nano Letters*, 2013.
- [14] G. Kucsko, P. C. Maurer, N. Y. Yao, M. Kubo, H. J. Noh, P. K. Lo, H. Park, and M. D. Lukin. Nanometre-scale thermometry in a living cell. *Nature*, 500(7460):54–58, 2013.
- [15] G. P. Conangla, A. W. Schell, R. A. Rica, and R. Quidant. Motion control and optical interrogation of a levitating single NV in vacuum. 2018.

- [16] T. D. Ladd, F. Jelezko, R. Laflamme, Y. Nakamura, C. Monroe, and J. L. O'Brien. Quantum computers. *Nature*, 464(7285):45–53, mar 2010.
- [17] David J. Wineland. Nobel Lecture: Superposition, entanglement, and raising Schrödinger's cat. *Reviews of Modern Physics*, 85(3):1103–1114, jul 2013.
- [18] I. M. M Georgescu, S. Ashhab, and Franco Nori. Quantum simulation. *Rev. Mod. Phys.*, 86(1):153–185, mar 2014.
- [19] V. M. Acosta, E. Bauch, M. P. Ledbetter, A. Waxman, L. S. Bouchard, and D. Budker. Temperature dependence of the nitrogen-vacancy magnetic resonance in diamond. *Physical Review Letters*, 104(7):1–4, 2010.
- [20] Marcus W. Doherty, Viktor V. Struzhkin, David A. Simpson, Liam P. McGuinness, Yufei Meng, Alastair Stacey, Timothy J. Karle, Russell J. Hemley, Neil B. Manson, Lloyd C. L. Hollenberg, and Steven Prawer. Electronic properties and metrology applications of the diamond nv^- center under pressure. *Phys. Rev. Lett.*, 112:047601, Jan 2014.
- [21] Wei Hong Wee, Zedong Li, Jie Hu, Nahrizul Adib Kadri, Feng Xu, Fei Li, and Belinda Pinguang-Murphy. Fabrication of dielectrophoretic microfluidic chips using a facile screen-printing technique for microparticle trapping. *Journal of Micromechanics and Microengineering*, 25(10):105015, 2015.
- [22] Viva R. Horowitz, Benjamín J. Alemán, David J. Christle, Andrew N. Cleland, and David D. Awschalom. Electron spin resonance of nitrogen-vacancy centers in optically trapped nanodiamonds. *Proceedings of the National Academy of Sciences*, 109(34):13493–13497, aug 2012.
- [23] Onofrio M. Maragò, Philip H. Jones, Pietro G. Gucciardi, Giovanni Volpe, and Andrea C. Ferrari. Optical trapping and manipulation of nanostructures. *Nature Nanotechnology*, 8(11):807–819, nov 2013.
- [24] Michael Geiselmann, Mathieu L. Juan, Jan Renger, Jana M. Say, Louise J. Brown, F. Javier García de Abajo, Frank Koppens, and Romain Quidant. Three-dimensional optical manipulation of a single electron spin. *Nature Nanotechnology*, 8(3):175–179, mar 2013.
- [25] Levi P. Neukirch, Jan Gieseler, Romain Quidant, Lukas Novotny, and A. Nick Vamivakas. Observation of nitrogen vacancy photoluminescence from an optically levitated nanodiamond. 38(16):2976–2979, 2013.
- [26] Reece P. Roberts. *Quantum-optical trapping of nanodiamonds containing NV centres*. PhD thesis, 2014.
- [27] Thai M. Hoang, Jonghoon Ahn, Jaehoon Bang, and Tongcang Li. Electron spin control of optically levitated nanodiamonds in vacuum. *Nature Communications*, 7:12250, jul 2016.
- [28] David Hempston, Jamie Vovrosh, Marko Toroš, George Winstone, Muddassar Rashid, and Hendrik Ulbricht. Force sensing with an optically levitated charged nanoparticle. *Applied Physics Letters*, 111(13):1–5, 2017.
- [29] Levi P. Neukirch, Eva Von Haartman, Jessica M. Rosenholm, and A. Nick Vamivakas. Multi-dimensional single-spin nano-optomechanics with a levitated nanodiamond. *Nature Photonics*, 9(10):653–657, 2015.
- [30] Tom Delord, Louis Nicolas, Lucien Schwab, and Gabriel Hétet. Electron spin resonance from NV centers in diamonds levitating in an ion trap. 2016.
- [31] T. Delord, L. Nicolas, Y. Chassagneux, and G. Hétet. Strong coupling between a single nitrogen-vacancy spin and the rotational mode of diamonds levitating in an ion trap. *Physical Review A*, 96(6):1–7, 2017.
- [32] D. Leibfried, R. Blatt, C. Monroe, and D. Wineland. Quantum dynamics of single trapped ions. *Reviews of Modern Physics*, 75(1):281–324, 2003.
- [33] T. Delord, P. Huillery, L. Schwab, L. Nicolas, L. Lecordier, and G. Hétet. Ramsey interferences and spin echoes from electron spins inside a levitating macroscopic particle. pages 1–16, 2018.

- [34] C. E. Pearson, D. R. Leibrandt, W. S. Bakr, W. J. Mallard, K. R. Brown, and I. L. Chuang. Experimental investigation of planar ion traps. *Physical Review A*, 73(3):032307, mar 2006.
- [35] Roman Schmied. Electrostatics of gapped and finite surface electrodes. *New Journal of Physics*, 12(3), 2010.
- [36] Manuel Mielenz, Henning Kalis, Matthias Wittemer, Frederick Hakelberg, Ulrich Warring, Roman Schmied, Matthew Blain, Peter Maunz, David L Moehring, Dietrich Leibfried, and Tobias Schaetz. Arrays of individually controlled ions suitable for two-dimensional quantum simulations. *Nature Communications*, 7:ncomms11839, jun 2016.
- [37] Sébastien Bourdeauducq, Robert Jördens, Peter Zotov, Joe Britton, Daniel Slichter, David Leibrandt, David Allcock, Aaron Hankin, Florent Kermarrec, Yann Sionneau, Raghavendra Srinivas, Ting Rei Tan, and Justin Bohnet. *Artiq 1.0*, May 2016.
- [38] Julia Tisler, Gopalakrishnan Balasubramanian, Boris Naydenov, Roman Kolesov, Bernhard Grotz, Rolf Reuter, Jean-paul Boudou, Patrick A Curmi, Mohamed Sennour, Alain Thorel, Michael Bo, Kurt Aulenbacher, Rainer Erdmann, Philip R Hemmer, and Fedor Jelezko. Fluorescence and Spin Properties of Defects in Single Digit Nanodiamonds. 3(7):1959–1965, 2009.
- [39] M Lesik. Engineering of NV color centers in diamond for their applications in quantum information and magnetometry. *Physics*, PhD, 2015.
- [40] A. Lenef, S. Brown, D. Redman, S. Rand, J. Shigley, and E. Fritsch. Electronic structure of the N-V center in diamond: Experiments. *Physical Review B - Condensed Matter and Materials Physics*, 53(20):13427–13440, 1996.
- [41] M. W. Doherty, N. B. Manson, P. Delaney, and L. C L Hollenberg. The negatively charged nitrogen-vacancy centre in diamond: The electronic solution. *New Journal of Physics*, 13, 2011.
- [42] M. W. Doherty, F. Dolde, H. Fedder, F. Jelezko, J. Wrachtrup, N. B. Manson, and L. C.L. Hollenberg. Theory of the ground-state spin of the NV - center in diamond. *Physical Review B - Condensed Matter and Materials Physics*, 85(20):1–21, 2012.
- [43] Kai-mei C Fu, Charles Santori, Paul E Barclay, Lachlan J Rogers, Neil B Manson, and Raymond G Beausoleil. Observation of the Dynamic Jahn-Teller Effect in the Excited States of Nitrogen-Vacancy Centers in Diamond. 256404(DECEMBER):1–4, 2009.
- [44] S. Felton, A. M. Edmonds, M. E. Newton, P. M. Martineau, D. Fisher, D. J. Twitchen, and J. M. Baker. Hyperfine interaction in the ground state of the negatively charged nitrogen vacancy center in diamond. *Physical Review B - Condensed Matter and Materials Physics*, 79(7):1–8, 2009.
- [45] David A. Broadway, James D. A. Wood, Liam T. Hall, Alastair Stacey, Matthew Markham, David A. Simpson, Jean-Philippe Tetienne, and Lloyd C. L. Hollenberg. Spin dynamics of diamond nitrogen-vacancy centres at the ground state level anti-crossing and all-optical low frequency magnetic field sensing. pages 1–10, 2016.
- [46] A. Gruber, A. Dräbenstedt, C. Tietz, L. Fleury, J. Wrachtrup, and C. Von Borczyskowski. Scanning confocal optical microscopy and magnetic resonance on single defect centers. *Science*, 276(5321):2012–2014, 1997.
- [47] Viktor Ivády, Tamás Simon, Jeronimo R. Maze, I. A. Abrikosov, and Adam Gali. Pressure and temperature dependence of the zero-field splitting in the ground state of NV centers in diamond: A first-principles study. *Physical Review B - Condensed Matter and Materials Physics*, 90(23):1–8, 2014.
- [48] D.F. Williams and S.E. Schwarz. Design and Performance of Coplanar Waveguide Band-pass Filters. *IEEE Transactions on Microwave Theory and Techniques*, 31(7):558–566, 1983.
- [49] Toptica Photonics. *ibema smart + smartdock*. [Online; accessed Nov 27, 2018].
- [50] M. Czerny and A. F. Turner. Über den astigmatismus bei spiegelspektrometern. *Zeitschrift für Physik*, 61(11):792–797, Nov 1930.

- [51] Microdiamant GMBH. Monocrystallizing micro-diamonds.
- [52] Taras Plakhotnik, Marcus W. Doherty, Jared H. Cole, Robert Chapman, and Neil B. Manson. All-optical thermometry and thermal properties of the optically detected spin resonances of the NV-center in nanodiamond. *Nano Letters*, 14(9):4989–4996, 2014.
- [53] Vladyslav O Shkolnikov, Adam Gali, and Guido Burkard. Spin-strain interaction in nitrogen-vacancy centers in diamond. (Section V):1–13.
- [54] E. van Oort, N. B. Manson, and M. Glasbeek. Optically detected spin coherence of the diamond N-V centre in its triplet ground state. *Journal of Physics C: Solid State Physics*, 21(23):4385, 1988.
- [55] Gopalakrishnan Balasubramanian, Philipp Neumann, Daniel Twitchen, Matthew Markham, Roman Kolesov, Norikazu Mizuochi, Junichi Isoya, Jocelyn Achard, Johannes Beck, Julia Tissler, Vincent Jacques, Philip R. Hemmer, Fedor Jelezko, and Jörg Wrachtrup. Ultralong spin coherence time in isotopically engineered diamond. *Nature Materials*, 8(5):383–387, may 2009.
- [56] P. L. Stanwix, L. M. Pham, J. R. Maze, D. Le Sage, T. K. Yeung, P. Cappellaro, P. R. Hemmer, A. Yacoby, M. D. Lukin, and R. L. Walsworth. Coherence of nitrogen-vacancy electronic spin ensembles in diamond. *Physical Review B*, 82(20):201201, nov 2010.
- [57] D. M. Toyli, D. J. Christle, A. Alkauskas, B. B. Buckley, C. G. Van de Walle, and D. D. Awschalom. Measurement and Control of Single Nitrogen-Vacancy Center Spins above 600 K. *Physical Review X*, 2(3):031001, jul 2012.
- [58] M. Kim, H. J. Mamin, M. H. Sherwood, K. Ohno, D. D. Awschalom, and D. Rugar. Decoherence of Near-Surface Nitrogen-Vacancy Centers Due to Electric Field Noise. *Physical Review Letters*, 115(8), 2015.
- [59] P. Jamonneau, M. Lesik, J. P. Tetienne, I. Alvizu, L. Mayer, A. Dréau, S. Kosen, J. F. Roch, S. Pezzagna, J. Meijer, T. Teraji, Y. Kubo, P. Bertet, J. R. Maze, and V. Jacques. Competition between electric field and magnetic field noise in the decoherence of a single spin in diamond. *Physical Review B*, 93(2):1–5, 2016.
- [60] R. Hanson, O. Gywat, and D. D. Awschalom. Room-temperature manipulation and decoherence of a single spin in diamond. *Physical Review B - Condensed Matter and Materials Physics*, 74(16):1–5, 2006.
- [61] P. C. Maurer, G. Kucsko, C. Latta, L. Jiang, N. Y. Yao, S. D. Bennett, F. Pastawski, D. Hunger, N. Chisholm, M. Markham, D. J. Twitchen, J. I. Cirac, and M. D. Lukin. Room-Temperature Quantum Bit Memory Exceeding One Second. *Science*, 336(6086):1283–1286, 2012.
- [62] Frederick Hakeberg, Philip Kiefer, Matthias Wittemer, Tobias Schaetz, and Ulrich Warring. Hybrid setup for stable magnetic fields enabling robust quantum control. *Scientific Reports*, 8(1):4404, 2018.
- [63] Robert Maiwald, Dietrich Leibfried, Joe Britton, James C. Bergquist, Gerd Leuchs, and David J. Wineland. Stylus ion trap for enhanced access and sensing. *Nature Physics*, 5(8):551–554, 2009.
- [64] Simon J. Gaskell. Electrospray: principles and practice. *Journal of mass spectrometry*, 32(7):677–688, 1997.

Acknowledgements

I thank Prof.Dr. Tobias Schaetz for his support throughout the thesis and allowing me to stay and work in his lab corridor. :)

I thank Dr. Ulrich Warring for guiding me, for being my lab buddy and allowing me to disturb him at any point of time for discussions.

I thank Prof.Dr. Tobias Schaetz again along with tutor Matthias Wittemer for the lecture Trapping, Cooling and Quantum control.

I thank Prof.Dr. Alexander Rohrbach, Prof.Dr. Guisuppe Sansone, Apl.Prof.Dr. Heinz-Peter Breuer for their lectures and constructive discussions.

I thank Joern Denter and Helga Mueller for sharing my burden in all sorts of administrative stuffs.

I thank Mr. Grossmann and his team for their support in making mechanical components for the experiments.

I thank Dr. Kambiz Mahboubi and his team for their support with electrical and electronic components(making and repairing).

I thank Oleg Orlev(preliminary Micro-strip) and Andre Cieluch for tolerating me as a colleague.

I thank my fellow group members for being supportive and helpful throughout my master thesis period.

I thank my family, sisters and friends for supporting me throughout my master thesis.